Effects of Implementing the Simple Biosphere Model in a General Circulation Model

N. SATO,* P. J. SELLERS, D. A. RANDALL,** E. K. SCHNEIDER, J. SHUKLA,
J. L. KINTER III, Y-T. HOU AND E. ALBERTAZZI

Center for Ocean–Land–Atmosphere Interactions, Department of Meteorology, University of Maryland, College Park, Maryland

(Manuscript received 5 May 1988, in final form 10 February 1989)

ABSTRACT

The Simple Biosphere Model (SiB) of Sellers et al. was designed to simulate the interactions between the Earth's land surface and the atmosphere by treating the vegetation explicitly and realistically, thereby incorporating the biophysical controls on the exchanges of radiation, momentum, sensible and latent heat between the two systems. This paper describes the steps taken to implement SiB in a modified version of the National Meteorological Center's global spectral general circulation model (GCM) and explores the impact of the implementation on the simulated land surface fluxes and near-surface meteorological conditions. The coupled model (SiB–GCM) was used to produce summer and winter simulations. The same GCM was used with a conventional hydrological model (Ctl–GCM) to produce comparable "control" summer and winter simulations for comparison.

It was found that SiB–GCM produced a more realistic partitioning of energy at the land surface than Ctl–GCM. Generally, SiB–GCM produced more sensible heat flux and less latent heat flux over vegetated land than did Ctl–GCM and this resulted in a much deeper daytime planetary boundary layer and reduced precipitation rates over the continents in SiB–GCM. In the summer simulation, the 200 mb jet stream was slightly weakened in the SiB–GCM relative to the Ctl–GCM results and analyses made from observations.

1. Introduction

This paper describes a study in which a simple but biophysically based model of the terrestrial vegetation was implemented in a general circulation model (GCM) of the atmosphere. The motivation for the study was to assess the impact of implementing such a scheme on the simulated climate with particular reference to (i) observations where available and, (ii) a parallel simulation produced with an abiotic land surface model.

Over the last decade, the scientific community has recognized that the interaction between the land surface and the atmosphere may play a significant role in the climate system; specifically, the fluxes of radiation, momentum and sensible and latent heat between the two systems may influence the atmospheric motion, temperature, humidity and precipitation fields which in turn feed back onto the spatial distribution of the sinks and sources of these fluxes on the land surface.

Until recently, the land surface properties which regulate the exchange of radiation, momentum and heat with the atmosphere have been regarded as separate items which may be independently prescribed as boundary conditions within a GCM. Although this approach is not very realistic, it lends itself to the investigation of land surface–atmosphere interactions by way of sensitivity studies conducted with GCMs. The three land surface properties which ultimately govern these interactions are the albedo (radiative transfer), surface roughness (momentum transfer) and the surface hydrological parameterization/prescription (sensible and latent heat transfer), all of which have been the subject of individual sensitivity studies.

First, the surface albedo is known to vary from about 12% (tropical rain forest) to around 35% (Sahara desert) over the snowfree land (Shuttleworth et al. 1984b; Matthews 1984). Charney et al. (1977) conducted a series of GCM sensitivity experiments centered on albedo changes in the Sahel which indicated that an increase in the albedo of the region would lead to a decrease in the surface evaporation rate and a reduction in the precipitation rate in the same area. This study was followed by similar ones on the Sahel/Sahara region (Sud and Fennessy 1982; Chervin 1979) which produced the same result qualitatively if not quantitatively. Carson and Sangster (1981) performed a more radical experiment by comparing two GCM simulations wherein the global land surface albedo, α, was prescribed as 0.1 or 0.3. The lower albedo case was associated with a greater precipitation rate over the land, (4.6 mm day^{-1} for $\alpha = 0.1$ and 3.4 mm day^{-1} for $\alpha = 0.3$).

* Japan Meteorological Agency, Chiyoda-ku, Tokyo, Japan.
** Dept. of Atmos, Sciences, Colorado State University, Fort Collins, Colorado.

Corresponding author address: Dr. Piers Sellers, Center for Ocean–Land–Atmosphere Interactions, University of Maryland, College Park, MD 20742.

© 1989 American Meteorological Society

The effect of changing the surface roughness length (z_0) fields was investigated by Sud and Smith (1985): the roughness length of the world's deserts was reduced from 45 cm to 0.2 mm which brought about changes in horizontal water vapor convergence and convective precipitation.

Many sensitivity studies have been devoted to investigating the role of land surface hydrology in the exchange of energy between the surface and the atmosphere. Walker and Rowntree (1977), Carson and Sangster (1981), Shukla and Mintz (1982), Warrilow (1986) and others reviewed in Mintz (1984) have performed experiments ranging from global prescriptions of totally wet versus totally dry land surfaces to alterations in regional soil moisture capacities. In almost all cases, reduced land surface evaporation rates led to reduced precipitation rates in the continental interiors.

All of these experiments served to demonstrate that the specification of albedo, roughness and the "surface wetness" could have important impacts on atmospheric fields. Dickinson (1984) therefore proposed that more realistic descriptions of land surface processes be incorporated in GCMs and designed a model which explicitly refers to the effects of vegetation. This has since been used for a simulation study of the climatic impact of large-scale deforestation of the Amazon basin (Dickinson and Henderson-Sellers 1988). Sellers et al. (1986) formulated the Simple Biosphere model (SiB) wich incorporates much of the philosophy of the Dickinson (1984) model while differing in detail. Both of these models have undergone sensitivity studies which indicate that their inclusion in GCMs should lead to more realistic and accurate calculations of the land surface–atmosphere fluxes (e.g., Sellers and Dorman 1987). This paper reports on a further study, in which the conventional land surface hydrology model used in a research version of the National Meteorological Center (NMC) GCM was replaced by SiB. Changes in the simulated surface and atmospheric fields as a result of this implementation are discussed with reference to relevant observations where available.

2. Description of the model and experiment design

A modified version of the National Meteorological Center (NMC) spectral GCM (Sela 1980) was used in the study. The dynamics formulation of the model is described in Sela (1980) and Kinter et al. (1988) describe the initialization procedures and boundary conditions used in the model. The model has a rhomboidal truncation at total wave number 40, Laplacian-square type horizontal diffusion to avoid spectral blocking and is discretized into 18 vertical levels of which the planetary boundary layer (PBL) may typically occupy five or six. It has a shallow convection scheme (Tiedtke et al. 1984) as well as a large-scale precipitation and cumulus convection scheme after Kuo (1965) which serves as a moist process parameterization. The model has three soil layers with prognostic temperatures at 2.5 cm, 10 cm, and 50 cm depth; the temperature at 500 cm is kept constant. The surface hydrology is represented by a bucket model (Manabe 1969) *wherein* the wetness is defined as the soil moisture divided by three quarters of the maximum soil moisture content, which is taken to be 150 mm on all land surfaces. These model "physics" were taken from the 1986 version of NMC medium range forecast model.

Some parameterizations were changed:

1) A more efficient radiation scheme was incorporated to permit the simulation of the diurnal cycle (Harshvardhan et al. 1987). The longwave radiation scheme is based on that of Harshvardhan and Corsetti (1984) and the shortwave (solar) radiation scheme is based on that of Lacis and Hansen (1974) as modified by Davies (1982). The solar radiation scheme was further modified to allow for partial cloudiness. The new longwave scheme has less spectral resolution than the preexisting scheme of Fels and Schwarzkopf (1975), but it is not thought that this simplification gives rise to serious errors. The shortwave and longwave radiation fluxes are calculated every hour and 3 hours, respectively.

2) The description of the aerodynamic resistances (or surface drag coefficient) for momentum and sensible/latent heat transfer between the lowest model layer and the surface was based on the Monin–Obukhov similarity theory as used in the E2-physics package of the Geophysical Fluid Dynamics Laboratory (GFDL) model (Miyakoda and Sirutis 1986). When the virtual temperature correction is neglected, the surface drag coefficient depends on only two nondimensional parameters, the Richardson number and z_r/z_0, where z_r is the height of the lowest model level and z_0 is the surface roughness length. A simple analytic function was developed that gives results close to those calculated with the original formulation (Sato et al. 1989). This function is used in order to avoid the costly iterations necessary for calculating the Monin–Obukhov length.

3) The level 2 second-order closure model of Mellor and Yamada (1982) was implemented as a parameterization of vertical diffusion in the PBL. This scheme has also been used in the GFDL spectral model (Miyakoda and Sirutis 1977) and in the fine-mesh grid model of the Japan Meteorological Agency (Yamagishi 1980). The eddy transfer coefficient was made a diagnostic function of Richardson number in this scheme.

4) The surface and PBL physics were coupled so that heat and mass exchanges between the surface and atmosphere satisfy energy and mass conservation laws. An implicit scheme with explicit coefficients was used with iteration to time-integrate the coupled system to eliminate numerical oscillation.

This modified version of the NMC GCM is referred to as the control model (Ctl–GCM) in this paper.

The hydrological model in Ctl–GCM is the same as that used in the NMC and GFDL GCMs. The scheme consists of a conceptual bucket for each land point, which is filled by precipitation and emptied by evaporation and runoff. The rate of evaporation is determined by the product of a potential evaporation rate, the rate that would result from a saturated surface with the same roughness and surface temperature, and a wetness value, which is taken as a simple linear function of the level of water in the bucket. The scheme has the attraction of being conceptually simple, but cannot be considered as a realistic description of the energy partition process as it actually occurs in nature. The most important omission of the bucket model is that of biophysical control of transpiration: vegetation can exert a considerable resistance on the transfer of water from soil to atmosphere and this can reduce the evapotranspiration rate to a level significantly below that calculated with the bucket formulation. Sellers (1987) discusses this and related shortcomings of the bucket model and concluded that it will almost always overestimate evaporation rates over the land. In this paper, we investigate the effect of replacing the conventional bucket hydrology model used in Ctl–GCM with the Simple Biosphere model (SiB) of Sellers et al. (1986). SiB directly addresses the effect of vegetation on land surface–atmosphere interactions by modeling those physiological and biophysical processes which influence radiation, momentum, mass and heat transfer.

The details of the implementation of SiB into the GCM are discussed in Sato et al. (1989). The complete SiB–GCM combination was then used to produce 50-day summer and 30-day winter simulations which were compared to equivalent simulations produced by Ctl–GCM. In both SiB–GCM and Ctl–GCM, the same boundary conditions for sea surface temperature (SST), sea ice distribution, initial snow amount and topography were used. The other land surface boundary conditions or parameters were treated differently in the two models.

Surface albedo in Ctl–GCM was interpolated from the seasonal climatology of Posey and Clapp (1964). In SiB–GCM the albedo is calculated with a vegetation canopy radiation model based on the two stream approximation (Sellers 1985) and depends on vegetation type and state and the solar zenith angle (Dorman and Sellers 1989). Over most of the continental areas except for north of 50°N, the Posey and Clapp (1964) albedo field is unrealistically low for reasons discussed in Dorman and Sellers (1989). The high albedo to the north of 65°N in Ctl–GCM is appropriate for snow-covered conditions. Regional values of surface albedo can be calculated from Table 1.

Surface roughness length, z_0, is time invariant in Ctl–GCM while in SiB–GCM it depends on the vegetation type and the month, see Dorman and Sellers (1989). The major differences between the models occur in the deserts of China and Mongolia: the roughness lengths there are around 30 cm in Ctl–GCM and 1 cm in SiB–GCM which may be compared to values of around 1 cm reported by Matthews (1984).

Up to now, the normal practice in Ctl–GCM has been to prescribe the global soil moisture field from a "climatological" dataset, thus effectively maintaining the wetness at or near its "climatological" value at every grid point. In Ctl–GCM, soil moisture contents were updated daily from climatology, but a test was also executed in which Ctl–GCM calculated the time evolution of the soil moisture. In SiB–GCM, soil moisture was predicted throughout all simulations.

TABLE 1. The mean surface energy budget as calculated by (a) Ctl–GCM, and (b) SiB—GCM for the four regions outlined in Fig. 1: Amazon Basin, Central and Eastern United States, Sahara Desert and Asia. The means are for the 50-day (15 June–4 August) summer simulations in all cases. The symbols used in the columns represent the following (all fluxes are in W m^{-2}). S: Insolation. $(1 - \alpha)S$: net short wave (absorbed by the surface). L_n: net longwave (absorbed by the surface). R_n: net radiation, available energy. λE_T: Transpired latent heat flux (SiB only). λE_I: interception loss plus soil evaporation latent heat flux (SiB only). λE: Total latent heat flux (sum of λE_T and λE_I in SiB). H: sensible heat flux. G: ground heat flux.

Region	S	$(1 - \alpha)S$	L_n	R_n	λE_T	λE_I	λE	H	G
a. Mean (50-day) surface energy budget calculated by Ctl–GCM.									
Amazon	211.1	194.8	−31.5	163.3	—	—	161.8	4.6	−3.1
Central and eastern United States	260.2	231.8	−34.9	196.9	—	—	176.4	18.4	2.1
Sahara desert	289.6	217.4	−92.4	125.0	—	—	3.1	117.1	4.8
Asia	281.9	236.6	−50.1	186.5	—	—	134.5	50.9	1.1
b. Mean (50-day) surface energy budget calculated by SiB–GCM.									
Amazon	210.9	184.7	−30.6	154.1	94.2	35.7	129.9	27.2	−3.0
Central and eastern United States	261.8	220.2	−39.9	180.3	114.9	20.1	135.0	41.1	4.2
Sahara desert	292.2	202.0	−83.1	118.9	3.36	.04	3.4	113.8	1.7
Asia	283.5	223.4	−54.0	169.4	93.2	18.0	111.2	57.4	0.8

These soil moisture and temperature initializations are discussed in Sato et al. (1989). Sellers et al. (1986) emphasized that the initialization of the soil moisture field is particularly problematical as it has a relatively long "memory;" the soil column in midlatitude zones is typically capable of storing a few hundred mm of water which translates to one or two months worth of evapotranspiration and runoff. The Ctl–GCM initial soil moisture fields were prepared by Willmott et al. (1985) using an hydrological budget method forced by observations of precipitation and air temperature. These fields were then transformed into equivalent SiB–GCM initial soil moisture fields by assuming that each matching pair of Ctl–GCM and SiB–GCM grid points had been exposed to the same history of evaporative demand up until the start of the run: see appendix D of Sato et al. (1989). The accuracy of these initial fields is questionable, a fact which is all the more disquieting as (i) it is certain that the soil moisture initialization can have a profound effect on the ensuing time-series of surface heat flux fields, and (ii) the simulation runs discussed in this paper are comparatively short. The obvious solution to the problem is to run both GCMs for several years in assimilation mode to generate self-consistent soil moisture climatologies, an option that was not available during this study due to constraints on computer time.

A final comment on the effects of the soil moisture initializations: within the upper range of soil wetness values; that is, greater than about 0.5, both models' responses are almost completely insensitive to the soil wetness (see Sellers and Dorman 1987). It is only when the soil moisture content drops below these values that we expect an impact on the calculated evapotranspiration rate. It will be shown in later discussion that the greatest differences between the land surface evaporation rates calculated by the two models occurred in zones with relatively high soil moisture contents.

The two GCMs, Ctl–GCM and SiB–GCM, were integrated for 50 days from 0000 UTC 15 June 1986, and 30 days from 0000 UTC 15 December 1985. The resulting simulated fields are compared to investigate the impact of including a biophysically based surface parameterization in a GCM. Particular attention has been paid to the differences in the surface hydrology and land surface energy budgets produced by the two models.

Two additional 30-day summer case experiments were made: a SiB–GCM run with a reduced soil moisture initialization in North America and a Ctl–GCM run in which the time evolution of the soil moisture was calculated rather than prescribed from climatology: see section 4b(2).

Following the completion of all the experiments, four coding errors were found; one in Ctl–GCM, one in SiB–GCM and two common to both models. In Ctl–GCM, the surface sensible heat flux was estimated by integrating the time rate of change in *virtual* temperature (rather than actual temperature) over the atmospheric column. This diagnostic error led to errors in the Ctl–GCM sensible heat flux fields on the order of 1%. In SiB–GCM, the moisture contribution to the virtual temperature time tendency due to vertical diffusion was treated incorrectly, which again is thought to lead to errors on the order of 1%. Third, eddy diffusivities in SiB–GCM and Ctl–GCM were four times as large as equivalent values obtained with the original Mellor–Yamada (1982) scheme. Last, in implementing the Mellor–Yamada (1982) code, the interlayer Richardson numbers were multiplied by a factor of two (relative to the original scheme) which leads to more rapid transitions from stable to unstable transfer conditions within the atmospheric column. This last error is common to both GCMs, but is not thought to have a severe impact on the simulations as for most of the time the transfer coefficients are operating in the "plateau" regions (i.e., stable or unstable conditions) where the eddy coefficients are not sensitive to the value of the Richardson number.

3. Overview of the Simple Biosphere Model (SiB)

Here we briefly review the structure, the atmospheric boundary conditions, the prognostic variables and the implementation of SiB.

a. Model philosophy

In most GCMs, including the original NMC GCM and Ctl–GCM, the fluxes of radiation, heat (sensible and latent) and momentum across the land surface–atmosphere boundary are conceptualized as largely separate processes, so that a given grid point has an independently specified albedo, an independently specified roughness length and an independently formulated dependence of evapotranspiration on soil moisture. This last generally takes the form of the bucket model described in the preceding section.

In designing the SiB model, the philosophy was to model the vegetation itself and thereby calculate the radiation, momentum, heat and mass transfer properties of the surface in a consistent way (Sellers et al. 1986). The morphological and physiological characteristics of the vegetation community at a grid point are used to derive coefficients and resistances which govern the fluxes between the surface and the atmosphere. All of these fluxes depend upon the state of the vegetated surface and the atmospheric boundary conditions.

In SiB, the world's vegetation is classified into twelve types or biomes: see Fig. 1. Detailed descriptions of the methods used to transform the morphological and physiological characteristics of a given vegetation type into the model parameters are given in Sellers et al. (1986) and the datasets and methodologies used to define the global distribution of vegetation types and attributes in SiB–GCM are reviewed in Dorman and Sellers (1989).

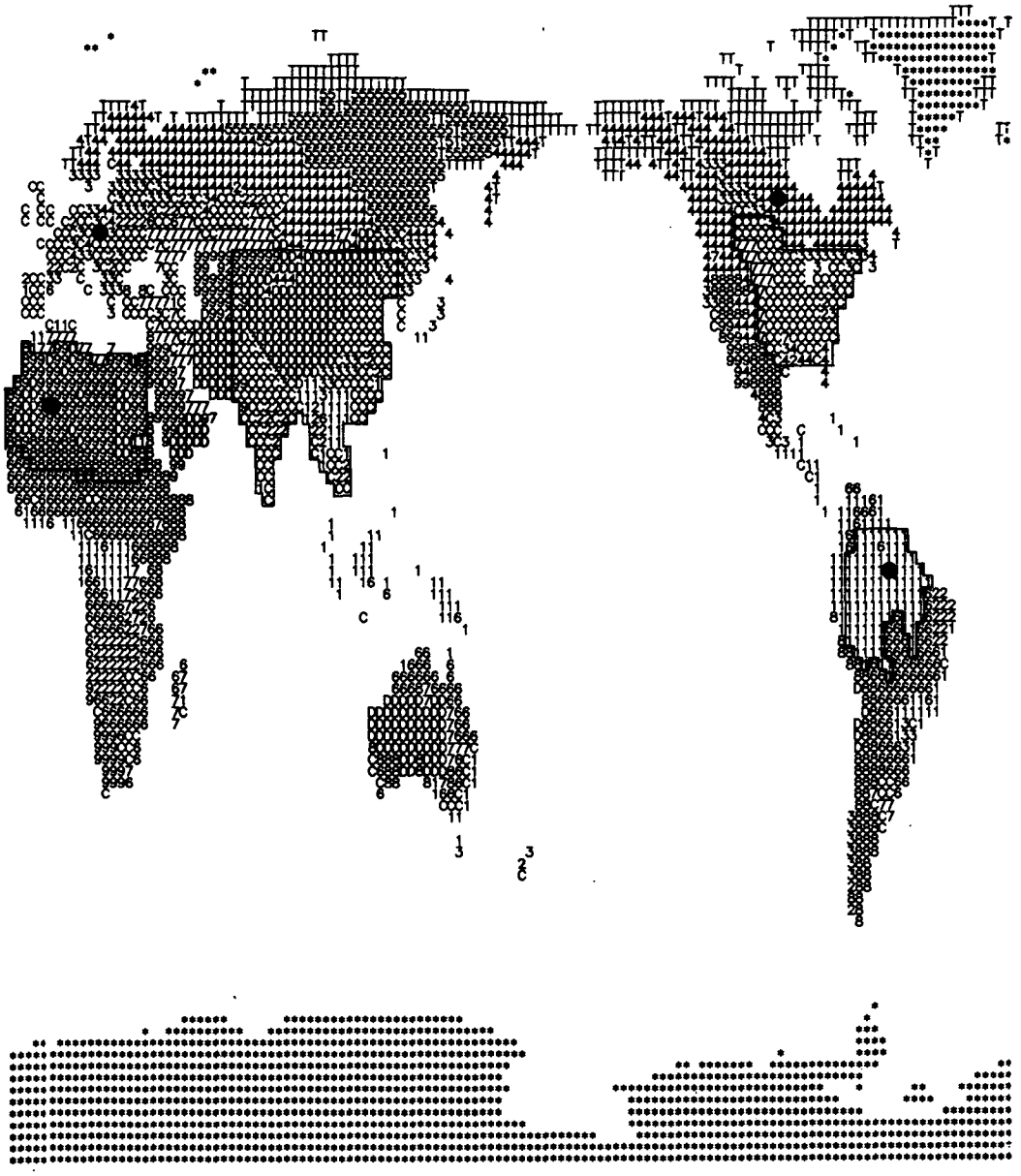

FIG. 1. Distribution of SiB vegetation types on the 128 × 102 Gaussian grid used in the NMC GCM: 1—broadleaf evergreen, 2—broadleaf deciduous, 3—mixed broadleaf deciduous and needleleaf evergreen, 4—needleleaf evergreen, 5—needleleaf deciduous, 6—grass and broadleaf deciduous shrubs, 7—grass, 8—broadleaf deciduous shrubs, growing singly, in patches or groups, 9—broadleaf deciduous shrubs, growing singly or in patches (semi-desert), T—tundra, D—desert, C—cultivated land represented by wheat, and *—glacier or permanent land ice cover. The sites used for the diurnal variation studies in section 4a are marked with solid dots. Energy and moisture budget analyses were made for the four areas encircled by solid lines: see section 4b.

b. Structure of the Simple Biosphere Model (SiB)

In SiB, the world's vegetation is divided into two morphological groups: trees or shrubs which constitute the upper story or canopy vegetation, and the ground cover which consists of grasses and other herbaceous plants. Either, both or neither of these vegetation covers may be present in a given grid area. The upper story vegetation consists of perennial plants with persistent roots assigned to a fixed depth taken to be the bottom of the second soil layer. The ground cover is made up of annual plants and may have a time-varying root depth. There is an upper, thin soil layer (soil layer 1), from which there can be a significant rate of withdrawal of water by direct evaporation into the air when the pores of the soil are at or near saturation. Beneath the root zone (soil layer 2), there is an underlying recharge layer (soil layer 3) where the transfer of water is gov-

erned only by gravitational drainage and hydraulic diffusion. The parameters required for each vegetation type in SiB are listed in Table 1 of Sellers et al. (1986). Values for many of the parameters are given in Dorman and Sellers (1989).

c. Atmospheric boundary conditions for SiB

The upper boundary conditions for SiB are as follows:

Air temperature, vapor pressure and wind speed of the lowest model layer,—T_m, e_m, u_m
The solar zenith angle—μ
Five components of the incident radiation—$F(0)$

- $F_{s,b(0)}$ Visible or PAR (<0.72 μm) direct beam radiation
- $F_{s,d(0)}$ Visible or PAR (<0.72 μm) diffuse radiation
- $F_{n,b(0)}$ Near infrared (0.72–4.0 μm) direct beam radiation
- $F_{n,d(0)}$ Near infrared (0.72–4.0 μm) diffuse radiation
- $F_{t,d(0)}$ Thermal infrared (8.0–12.0 μm) diffuse radiation

Large scale and convective precipitation rates—P_L, P_C.

d. Prognostic physical state variables of SiB and their governing equations

The SiB has eight prognostic physical-state variables: three temperatures (one for the canopy vegetation, T_c, one for both the ground cover and the soil surface, T_{gs}, and a deep soil temperature, T_d), two interception water stores (one for the canopy, M_c, and one for the ground cover, M_g), and three soil moisture stores (W_1, W_2 and W_3).

The governing equations for the three temperatures, T_c, T_{gs} and T_d, are given in Sellers et al. (1986) and Sato et al. (1989).

e. Implementation of SiB into the NMC Spectral Model

In the NMC model, the Mellor and Yamada (1982) vertical diffusion model at level 2 was incorporated. In this parameterization there are no explicit prognostic variables that describe the state of the PBL. The whole atmosphere, including the PBL, is discretized into layers and state variables such as temperature, specific humidity and wind velocity are defined and predicted on each level; specifically, temperature and wind are defined for all of the model's 18 levels while specific humidity is only defined for the 12 lowest levels (see Kinter et al. 1988). These atmospheric variables were coupled with the SiB prognostic variables, T_c and T_{gs}, so that energy and mass are conserved, and an implicit scheme is used to integrate the system stably in time. The other (slowly varying) SiB variables are integrated with a forward scheme. The original soil heat flux formulation described in Sellers et al. (1986) was replaced by the force–restore formulation of Deardorff (1977). The complete equation set and the solution technique may be found in Sato et al. (1989).

The Ctl–GCM uses the same basic time integration scheme. In Ctl–GCM, the atmospheric variables (temperature at 18 levels and specific humidity at 12 levels) were coupled with the ground surface temperature and soil temperatures at 10 cm and 50 cm depth. The system is integrated using the same implicit time integration scheme with explicit transfer coefficients. In order to integrate stably, iterations are made using a modified Newton–Raphson method.

As currently implemented, SiB has a significant impact on the computer time required for a simulation; SiB–GCM is typically 20% more expensive (computationally) than Ctl–GCM. However, it should be noted that no determined effort had been applied to make the code more efficient.

f. Anticipated impact of implementing SiB

The impact of implementing SiB into the GCM can be anticipated by comparing the surface parameterizations of SiB–GCM and Ctl–GCM.

First, there are some differences between the albedo field calculated by SiB–GCM and that prescribed in Ctl–GCM. Generally, the SiB–GCM albedos are significantly higher over vegetated regions, leading to reductions in the surface net radiation of around 5% in SiB–GCM relative to Ctl–GCM.

Second, there are some differences between the two roughness length fields, but these are not thought to contribute greatly to the differences between the performances of the two models except for the extreme cases referred to in the previous section (China, Mongolia). This is because the aerodynamic resistance is inversely related to the logarithm of the roughness length and so the turbulent heat flux calculations are relatively insensitive to fairly large changes in the absolute value of this parameter (see Sellers and Dorman 1987).

Third and most importantly, Ctl–GCM and SiB–GCM calculate the partition of energy at the surface in very different ways. The effect of this can be simply illustrated by comparing the energy budgets calculated by the two surface parameterizations for a densely vegetated area. If time-invariant forcing [T_m, e_m, u_m, $F(0)$] is assumed and the radiation budgets for the two models are taken as approximately equal, heat storage terms may be neglected and equilibrium surface fluxes and surface temperatures may be calculated with the two parameterizations. Under these conditions, the total energy budgets may be written as

$$R_n = H_B + \lambda E_B \quad (1a)$$

$$R_n = H_S + \lambda E_S \quad (1b)$$

where R_n is net radiation, W m^{-2}, H is sensible heat flux, W m^{-2}, E is evaporation rate, kg m^{-2} s^{-1}, and λ is latent heat of vaporization, J kg^{-1}. The subscripts B and S refer to the "bucket" and SiB parameterizations, respectively.

The sensible heat fluxes calculated by the two models are different due to the different equilibrium surface temperatures

$$H_B = \frac{(T_B - T_m)}{r_a} \rho c_p \tag{2a}$$

$$H_S = \frac{(T_S - T_m)}{r_a} \rho c_p \tag{2b}$$

where $T_{S,B}$ is surface temperature for SiB, bucket parameterization, K, ρ, c_p is density, specific heat of air, respectively; kg m^{-3}, J kg^{-1} K^{-1}, r_a is aerodynamic resistance between surface and lowest model layer, s m^{-1}, and is also $1/(C_H u_m)$, and C_H is heat transfer coefficient.

For Ctl–GCM, the evaporation rate is given by the so-called "Beta-function."

$$\lambda E_B = \beta \frac{(e^*(T_B) - e_m)}{r_a} \frac{\rho c_p}{\gamma} \tag{3a}$$

where $e^*(T)$ is saturated vapor pressure at temperature T, kPa, γ is psychrometric constant, kPa K^{-1}, (0.066 kPa K^{-1} at 15°C), β is $W/(0.75\ W_{\max})$, $0 \leq \beta \leq 1$, W is soil moisture content, mm, $W_{\max}$ is maximum value of W, and is 150 mm.

In SiB, the calculation of evapotranspiration is fairly complex, involving treatments for two layers of vegetation and the evaporative contribution from the bare soil. However, for a dense vegetation canopy, like a tropical forest, the evapotranspiration rate can be approximated by

$$\lambda E_S = \left[\frac{e^*(T_S) - e_m}{r_a + r_c}\right] \frac{\rho c_p}{\gamma} \tag{3b}$$

where r_c is the bulk stomatal (canopy) resistance, s m^{-1}.

The essential term in Eq. (3b) is r_c, the bulk stomatal or canopy resistance of the dry vegetation.

Equations (1), (2), and (3) can be combined and the surface temperatures, T_S and T_B, eliminated using the linear approximation for saturated vapor pressure as a function of temperature as shown in Monteith (1973) to yield

$$\lambda E_B = \frac{\Delta R_n + \rho c_p \delta e / r_a}{\Delta + \gamma/\beta} \tag{4a}$$

$$\lambda E_S = \frac{\Delta R_n + \rho c_p \delta e / r_a}{\Delta + \gamma[(r_a + r_c)/r_a]} \tag{4b}$$

where δe $(=e^*(T_m) - e_m)$ is vapor pressure deficit, kPa, and Δ (=0.11 kPa K^{-1} at 15°C) is the slope of saturated vapor pressure versus temperature curve at temperature T_m, kPa K^{-1}.

Equation (4b) is simply the Penman–Monteith evapotranspiration equation, see Monteith (1973). For the same meteorological (T_m, e_m, u_m) and radiative (R_n) forcings, the ratio of the calculated evapotranspiration rates is then given by

$$\frac{E_B}{E_S} = \frac{\Delta + \gamma[(r_a + r_c)/r_a]}{\Delta + \gamma/\beta} \tag{5}$$

For a tropical forest site, r_a is typically 10 s m^{-1} and, if soil moisture is not limiting, $\beta = 1$ and $r_c \approx 100$ s m^{-1}: see Shuttleworth et al. (1984a,b), which yields a value of $E_B/E_S = 4.75$! Furthermore, to obtain $E_B/E_S = 1$, β must be reduced to 0.091 which implies a soil wetness of $W = 0.07$, clearly below the range of reasonable "tuning" for a humid region.

The above analysis is extreme as it assumes that there is no feedback from the surface evaporation rate on the atmospheric forcing. In Ctl–GCM, the huge latent heat fluxes calculated in the first few timesteps should bring about an unrealistically cold, stable and humid PBL which then reduces subsequent evaporation rates to less extreme values. Nonetheless, we should expect to see marked differences between the surface heat fluxes calculated by the two models with associated differences in their near-surface climates.

4. Comparison of simulations as produced by control and SiB versions of the NMC GCM.

In this section, the simulations generated by the SiB–GCM and Ctl–GCM runs are compared with each other and with observations over a range of spatial scales.

First, analyses of surface and near-surface processes for representative grid points within each model (Fig. 1) are compared with equivalent field measurements. In particular, the 30-day (15 June–14 July) means of the simulated hourly net radiation, sensible heat and latent heat fluxes for a tropical forest, a coniferous forest and an agricultural site are compared with observations (section 4a).

Second, the simulated time series of the energy and moisture budgets of four large regions (the Amazon basin, central and eastern United States, southern Asia and the Sahara, see Fig. 1) are discussed with reference to observations where available (section 4b).

Third, the global fields of latent heat flux (evapotranspiration), sensible heat flux and precipitation generated by SiB–GCM and Ctl–GCM are compared (section 4c).

Fourth and last, the impacts of the two land surface parameterization schemes on the large-scale atmospheric circulation are discussed (section 4d).

a. Diurnal variation of surface and near-surface processes

Time series of fluxes and other variables for several grid points over the globe were examined to see how the implementation of SiB affects the diurnal variation of surface and PBL processes. The first 30 days of the SiB–GCM and Ctl–GCM (boreal) summer runs were analyzed for this study; 30 rather than 50 days were used as the surface energy budget changed in a spatially heterogeneous way in the last 20 days of the Ctl–GCM run.

1) TROPICAL RAIN FOREST, AMAZON BASIN

Figures 2 through 5 show 30-day means of the simulated diurnal variation of various physical parameters at a tropical forest grid point near Manaus in the Amazon basin (59°W, 3°S) for the period 15 June–14 July. Some equivalent observations from Shuttleworth et al. (1984a,b) for the same area are also shown for comparison.

In SiB–GCM the albedo is computed using a two-stream approximation model (Sellers 1985) which calculates the dependency of the albedo on the solar zenith angle. The minimum albedo at noon, (11.5%), and the daily mean albedo (12.6%) as calculated by SiB–GCM agree well with the observations made over the Amazon forest (Shuttleworth 1984b); 11.0 and 12.5% respectively. The albedo of 7% used in Ctl–GCM (Posey and Clapp 1964) is a climatological one and is unrealistically small for the reasons discussed in Dorman and Sellers (1989).

Because the albedos are different, there is a slight difference between the net radiation values calculated by SiB–GCM and Ctl–GCM (Figs. 2a, b); but the peak observed net radiation is 50–100 W m^{-2} less than either of the simulated values. However, the observed net radiation was always smaller than the sum of the observed latent and sensible heat fluxes which suggests that there may be some errors in the observed heat fluxes and/or net radiation values. Additionally, it is possible that the fixed zonal mean climatological cloudiness used in both GCMs leads to systematic errors in the simulations.

The heat flux into the soil is not shown in Figs. 2a and 2b. Typically, this term is calculated to be around 20 W m^{-2} during the day and −20 W m^{-2} at night. The daily mean value is very small and is an insignificant part of the surface energy budget in both models.

Figures 2a and 2b illustrate the improvement of the simulated surface energy budget due to the implementation of SiB–GCM. The simulations may be directly compared with the observations: 30 days (15 June–14 July) of the Shuttleworth et al. (1984a) dataset were averaged to produce the observed hourly fluxes shown in Figs. 2a and 2b. In SiB–GCM (Fig. 2a) the maximum values of latent heat flux, 380 W m^{-2}, and sensible heat flux, 170 W m^{-2}, agree fairly well with these observations. In Ctl–GCM (Fig. 2b), however, almost all of the net radiation is used for evaporation while the sensible heat flux is almost zero.

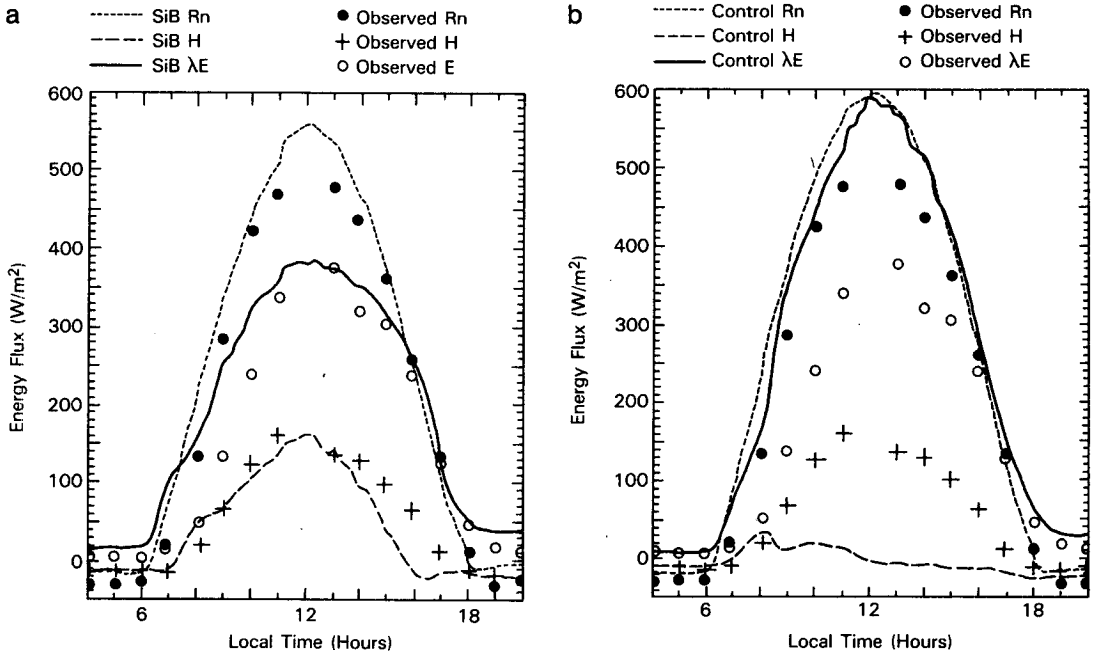

FIG. 2. (a) 30-day (15 June–14 July) mean surface energy balance at Manaus (3°S, 59°W) simulated by SiB and as observed by Shuttleworth et al. (1984a). The lines on the figure represent simulation, the points (circles and crosses) represent the means of observations taken from a site at 30 km from Manaus, Brazil. (b) As in Fig. 2a, except that the simulation was performed by Ctl–GCM.

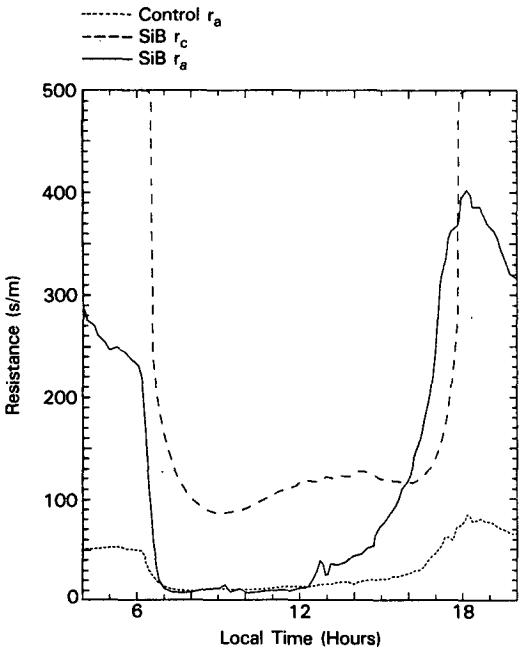

FIG. 3. The 30-day (15 June–14 July) mean surface (stomatal) and aerodynamic resistances at Manaus simulated by SiB–GCM and Ctl–GCM. r_a is aerodynamic resistance; r_c is surface (stomatal) resistance for the forest canopy in SiB. There is no equivalent to r_c in Ctl–GCM.

This unrealistic partitioning of net radiation in Ctl–GCM is a direct consequence of using the bucket model parameterization of surface evaporation. In the bucket model, the atmosphere is directly connected to the surface by the aerodynamic resistance which is relatively small when the surface layer is neutral or unstable, see Eq. (3a). In SiB–GCM, the transpired water also has to traverse the stomatal resistance which is typically one order of magnitude larger than aerodynamic resistance over the Amazon forest, see Eq. (3b). (In both SiB–GCM and Ctl–GCM, sensible heat fluxes are only regulated by the aerodynamic resistances). The diurnal variation of these resistances is shown in Fig. 3. The morning and midday values of the aerodynamic resistance, r_a, are around 10 s m^{-1} in both SiB–GCM and Ctl–GCM, but the stomatal resistance, r_c, plus leaf boundary layer resistance, r_b, in SiB–GCM never drops below 100 s m^{-1}. According to Shuttleworth et al. (1984a), daytime values of the aerodynamic resistance, r_a, estimated from eddy correlation data, frequently dropped to around 10 s m^{-1} and the mean minimum value of the canopy resistance, for the tropical forest was estimated to be around 130 s m^{-1} from the flux observations. The SiB–GCM simulations of r_a and $r_b + r_c$ concur with these observations. Additionally, a "bump" in the diurnal course of the stomatal resistance, centered on 1100–1200 local time, may also be

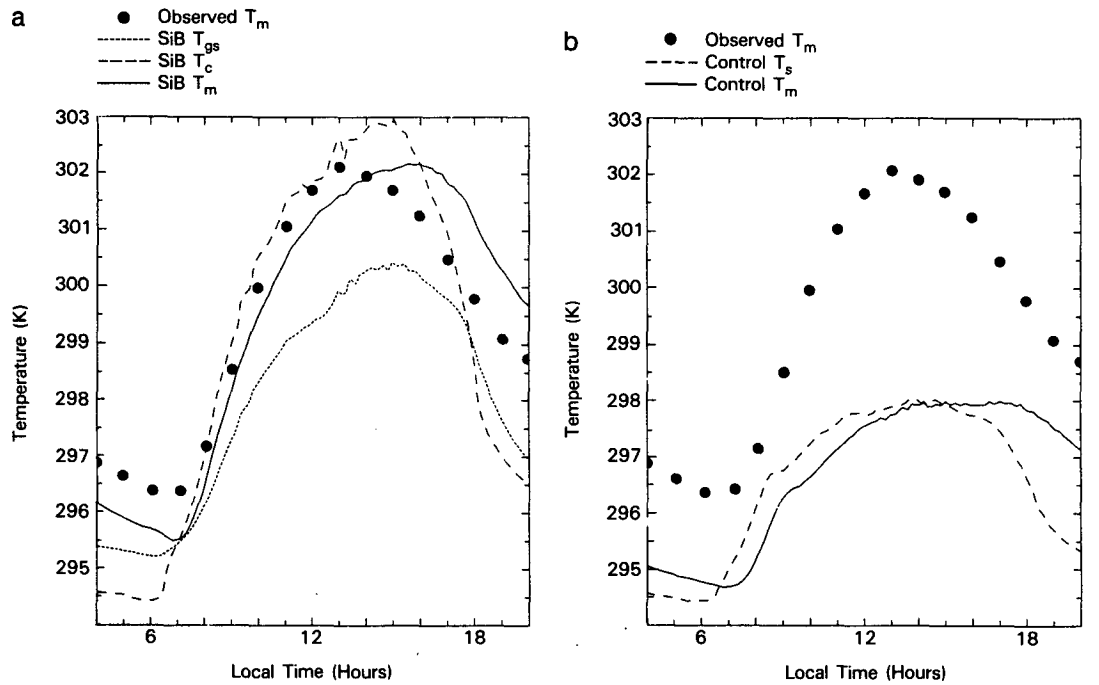

FIG. 4. (a) 30-day (15 June–14 July) mean air and surface temperatures at Manaus simulated by SiB–GCM. The solid line is for the temperature at the lowest model atmospheric level, T_m ($\sigma = 0.995$), the coarse dashed line is for the canopy temperature, T_c, and the dotted line is for the ground cover/surface temperature, T_{gs}. The series of solid dots represent the 30-day mean hourly air temperatures 45 m above ground (10 m above canopy top) as observed by Shuttleworth et al. (1984a) at Manaus. (b) 30-day (15 June–14 July) mean air and surface temperatures at Manaus simulated by Ctl–GCM. The solid line is for the temperature at the lowest model level ($\sigma = 0.995$), T_m, and the dashed line is for the ground surface temperature, T_s. The series of solid dots represent 30-day mean hourly air temperatures at 45 m above ground (10 m above canopy top) as observed by Shuttleworth et al. (1984a) at Manaus.

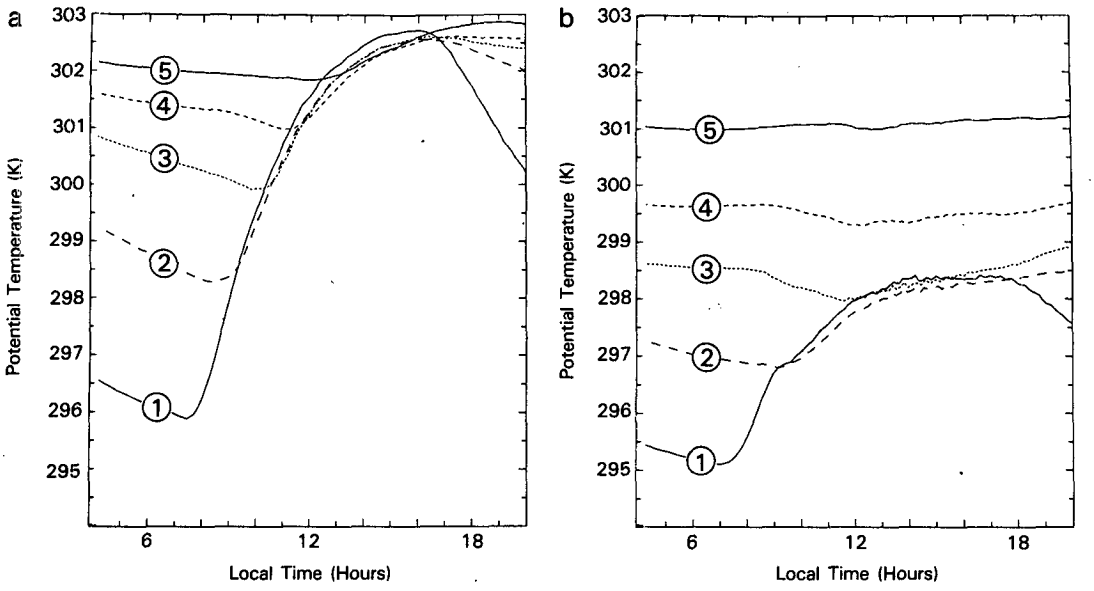

FIG. 5. (a) Simulated 30-day (15 June–14 July) mean hourly potential temperatures for the lowest five model levels (σ – 0.9950, 0.9815, 0.9605, 0.9205, 0.8565) at Manaus from SiB–GCM. (b) As in Fig. 5a, but for Ctl–GCM.

seen in Fig. 3. This feature corresponds to the midday depression in stomatal conductance and photosynthesis as observed in Oak shrub by Tenhunen et al. (1984) and is caused by the vegetations' response to the elevated temperatures and raised vapor pressure deficit in the canopy air space at this time of day. The reproduction of this feature indicates that the SiB–GCM is realistically simulating the coupled system of biological and near-surface meteorological processes.

Because of stomatal resistance, SiB–GCM generates more sensible heat than Ctl–GCM in most vegetated areas; this is associated with higher values and a larger diurnal range of surface temperatures in SiB–GCM. Figure 4a shows the SiB canopy, ground surface and air temperature for the lowest GCM level. Figure 4b shows corresponding results for Ctl–GCM: ground surface temperature and the air temperature of the lowest atmospheric level are shown. The monthly mean air temperature 44.6 m above the ground (average canopy top height was 35 m) as observed by Shuttleworth et al. (1984a,b) is shown in both figures. The observed temperature reaches 302 K with a diurnal range of about 6°K; the equivalent simulated values from SiB–GCM, 302 K 6.5°K respectively, are comparable to the observed values and are more realistic than the values calculated by Ctl–GCM (298 K and 3°K). The peak value of T_m calculated by SiB–GCM occurs two hours later than in the observations; this may be due to overly efficient vertical mixing in the lower layers of the model during the morning and midday periods.

The large sensible heat flux generated by SiB–GCM also helps the PBL to grow deeper and make the transport of heat, moisture and momentum flux within the PBL more efficient. Figures 5a and 5b show the calculated 30-day mean diurnal variation of potential temperature for the five lowest GCM levels (σ = 0.9950, 0.9815, 0.9605, 0.9205, 0.8565) in SiB–GCM and Ctl–GCM, respectively. With SiB–GCM the simulated PBL grows up to level 4 (i.e., the PBL depth is about 80 mb) and sometimes up to level 5 (150 mb). In the Ctl–GCM simulations, PBL growth in the area is capped at the third level which means that the PBL depth does not exceed 20 mb. Martin et al. (1988) observed the PBL structure over the Amazonian forest near Manaus for the three week period, 15 July–7 August 1985, during which the PBL depth grew to about 170 mb (1600 m) on fine days and 80 to 90 mb (800 m) on cloudy days. On the average, the maximum PBL depth was about 130 mb (1200 m) which agrees more closely with the SiB–GCM simulation.

The more unstable daytime conditions associated with the SiB–GCM simulation give rise to shear stresses which are roughly double those generated by Ctl–GCM; the 30-day mean maximum daily shear stresses are 0.28 and 0.17 Pa, respectively. These figures may be compared with the friction velocity measurements reported in Shuttleworth et al. (1984a), which are equivalent to shear stress values ranging from 0.01 Pa (nighttime, dawn, dusk) to over 0.5 Pa (midday, unstable conditions). These higher shear stresses are probably associated with moderately large sensible heat fluxes, consistent with the SiB–GCM calculation.

2) CONIFEROUS FOREST

Figure 6a (6b) shows the SiB–GCM (Ctl–GCM) simulations of latent and sensible heat flux for a grid

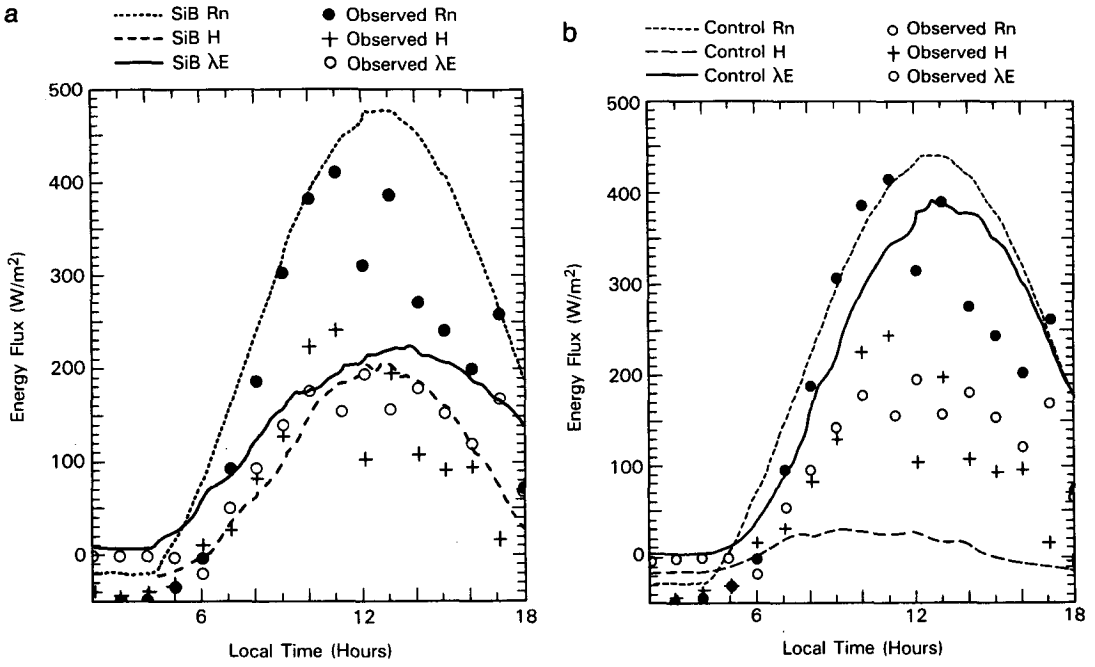

FIG. 6. (a) 30-day (15 June–14 July) mean surface energy balance for an evergreen coniferous forest grid area (55°N, 98°W) in central Canada as simulated by SiB–GCM. The points marked on the figure are for equivalent quantities as measured by McNaughton and Black (1973) over a Douglas fir forest in British Columbia on 20 July 1970. (b) As in Fig. 6a, except that the simulation was performed by Ctl–GCM.

point in Canada (55°N, 98°W); this point is represented as evergreen coniferous forest in SiB–GCM. As before, the means for the first 30 days (15 June–14 July) of the Northern Hemisphere summer simulations are shown. Estimated fluxes for one day at a coniferous forest site in Western Canada calculated from observations by McNaughton and Black (1973) are shown in both figures. On five other days in July 1970 the observed net radiation, latent and sensible heat fluxes were larger but the Bowen ratio was always around unity during the day. The simulated Bowen ratio in SiB–GCM is also very close to unity during the day whereas in Ctl–GCM it is near zero.

3) Cultivated area, Central Europe

Figure 7a (7b) shows the latent and sensible heat fluxes for a grid point at (49°N, 17°E), a cultivated area in Central Europe, as simulated by SiB–GCM (Ctl–GCM). Observed fluxes recorded over a barley field at Ruthe in West Germany on 20–22 June 1979 are also shown (van der Ploeg et al. 1980). As in the case of the Amazon rain forest and the evergreen coniferous forest in Canada, Ctl–GCM generates far too much latent heat flux whereas the time series of latent heat flux in SiB–GCM compares well with observations. The net radiation calculated by Ctl–GCM is also higher than that of SiB–GCM. This is mainly the result of the low albedo used in Ctl–GCM for the region; 12–13% as compared to values of 17% (midday) to 25% (dawn, dusk) calculated by SiB–GCM. The absolute values and diurnal variation of the SiB–GCM albedo appear to agree well with field observations (Sellers and Dorman 1987).

4) Sahara Desert

The 30-day mean maximum ground surface temperatures for the Sahara grid point (23°N, 0°E) were 327 K for Ctl–GCM and 325 K for SiB–GCM; the difference is probably due to the slightly higher albedo used in SiB–GCM.

Susskind (personal communication) retrieved daytime (1430 LT) and nighttime (0230 LT) ground surface temperatures from satellite data for the same area. The estimated daytime and nighttime temperatures for (23°N, 0°E) for July 1979 were 324 K and 296 K, respectively, which gives a diurnal range of 28°K. These may be compared with the equivalent simulated daytime ground surface temperatures of 326.5 K in Ctl–GCM and 323 K in SiB–GCM. The nighttime temperatures, 310 K in Ctl–GCM and 305 K in SiB–GCM, seem to be too high compared with observations even when uncertainties in the retrieval procedure are taken into account. One possible explanation is that the fixed zonal mean clouds in the GCMs reduced the amount of nocturnal cooling over the deserts. Excessive downward sensible heat flux from the atmosphere to the

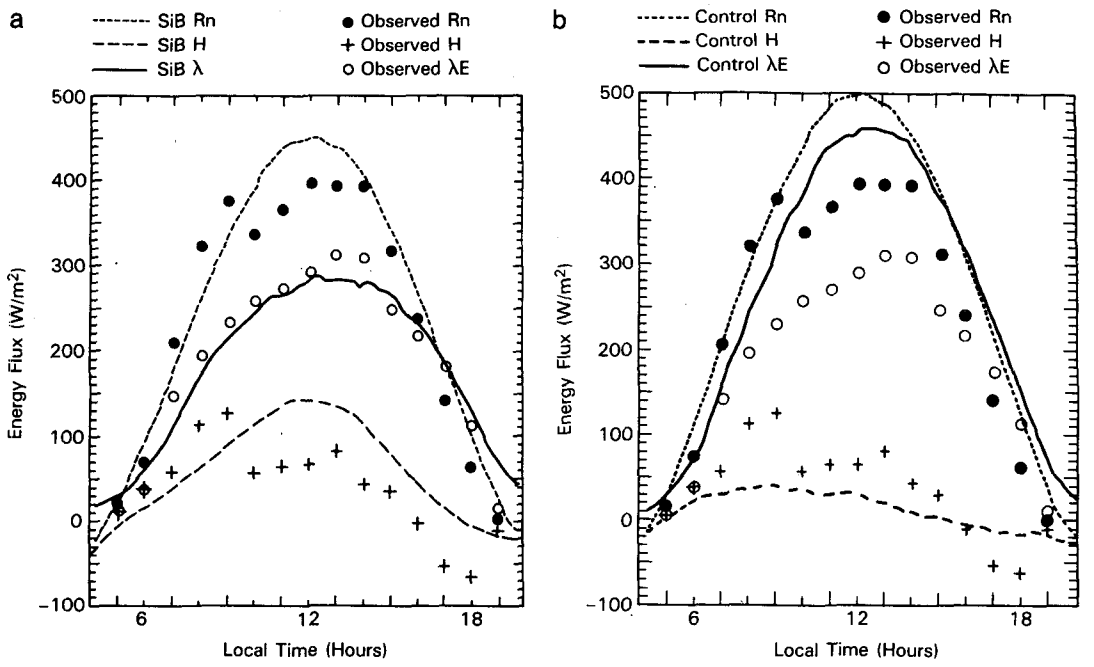

FIG. 7. (a) 30-day (15 June–14 July) mean surface energy balance for a cultivated grid area (49°N, 17°E) in central Europe as simulated by SiB–GCM. The points marked on the figure are for equivalent quantities as measured by van der Ploeg et al. (1980) over a barley field on 20–22 June 1979. (b) As in Fig. 7a, except that the simulation was performed by Ctl–GCM.

surface or heat conducted from the deep soil layer may also contribute to the higher nighttime ground surface temperatures.

b. Time tendency of regional mean energy and moisture budgets

Area-averaged budget analyses were made for 50 days (15 June–4 August) of summer simulations by both GCMs to find out how the regional energy and moisture budgets changed during the course of the numerical simulations. Four continental regions were selected: the Amazon basin, central and eastern United States, Asia, and the Sahara desert (Fig. 1).

In SiB–GCM, the Amazon basin is uniformly covered by tropical rain forest; the central and eastern United States consists mainly of cultivated land, grassland and some mixed forest; the Asian region consists of heterogeneous land cover including tropical rain forest, cultivated land and desert; and the Sahara consists of desert with a very sparse shrub cover.

1) ENERGY BUDGET

The mean daily surface energy budgets for the four regions as simulated by SiB–GCM and Ctl–GCM are shown in Table 1. The assumption of a fixed zonal mean climatological cloudiness and ozone distribution results in very similar surface insolations for the two models and very small day to day fluctuations of all components of the surface energy budget. For the Amazon basin, this mean value, 210 W m^{-2}, is larger than the July climatological value, 195 W m^{-2}, given by Budyko (1974). There is some difference in net solar radiation between the GCMs because of the different albedos used; 12.4% in SiB–GCM and 7.7% (Posey and Clapp 1964) in Ctl–GCM. This albedo difference results in a 10 W m^{-2} or a 5% difference in the net radiation.

The striking improvement of SiB–GCM over Ctl–GCM is shown in the partition of net radiation into latent and sensible heat fluxes. In the Ctl–GCM simulation for the Amazon region, almost all of the net radiation is used for evaporation and so the sensible heat flux is negligible. In the SiB–GCM simulation, 84% of the net radiation goes to latent heat flux giving a Bowen ratio of 0.21. This difference results from the different formulations used to calculate evapotranspiration in the two GCMs, see section 3f.

The latent heat fluxes, 130 W m^{-2} (SiB–GCM) and 162 W m^{-2} (Ctl–GCM), correspond to 4.5 mm day^{-1} (SiB–GCM) and 5.5 mm day^{-1} (Ctl–GCM) of evapotranspiration. Salati (1987) summarized published estimates of the mean annual evapotranspiration rate for the entire Amazon Basin to give a figure in the range of 3.1 to 4.0 mm day^{-2}. Even if we take the uncertainty of this estimate and seasonal variation into consideration, the evaporation rate given by SiB–GCM, 4.5 mm day^{-1}, is in better agreement with this estimate than Ctl–GCM.

The interception loss calculated for the Amazon by SiB–GCM is also shown in Table 1. (Interception loss refers to the precipitation that is intercepted by the

canopy and reevaporated back to the atmosphere without entering the soil). The time-averaged value, 36 W m^{-2}, represents 28% of the total evapotranspiration. Shuttleworth et al. (1984a) estimated an equivalent value of about 30% from their measurements taken at a site outside Manaus. An annual mean value of 35% was reported in Salati (1987) for a small basin (25 km^2) 60 km north of Manaus. Salati (1987) also mentions the report of Franken et al. (1982) which gives a value of 33% for a one-year period at another site 40 km from Manaus. In general then, the interception loss rate calculated by SiB–GCM seems to be realistic when compared to the observations. This could be partly due to the formulation used to account for the hydrological effects associated with the nonuniform spatial distribution of convective rainfall (appendix C in Sato et al. 1989).

There are large differences between the daily mean surface energy budgets for the central and eastern U.S. region as calculated by the two models: see Table 1. The calculated downward solar radiation at the surface is 260 W m^{-2} which is less than the climatological value of 275 W m^{-2} given by Budyko (1974) and Sellers (1965). The small difference in net radiation, 20 W m^{-2}, comes partly from the higher albedo in SiB–GCM versus Ctl–GCM, 16% vs 11%, and partly from the increased net longwave radiation flux associated with the higher surface temperature and drier PBL in SiB–GCM. As in the case of the Amazon basin, the major difference between the SiB–GCM and Ctl–GCM results is to be found in the partition of the net radiation into sensible and latent heat fluxes: the Bowen ratio is 0.3 in SiB–GCM and 0.1 in Ctl–GCM.

In Ctl–GCM, there is an increase in the sensible heat flux and a decrease in the latent heat flux toward the end of the 50-day summer simulation which is a result of a progressive reduction in the prescribed climatological soil moisture content. Figure 9b shows how the (prescribed) Ctl–GCM soil moisture decreased from 0.88 to 0.45 over the 50 days. In the parallel SiB–GCM run, the equivalent (prognostic) soil wetness (Fig. 9a) decreased very slowly, changing from 0.70 to 0.65 in 50 days. One reason for this relatively slow change in soil moisture is that SiB generally has a greater soil moisture capacity than the bucket model: The total depth of the moisture carrying zones is typically 1490 mm, porosity is 0.46 and the initial soil wetness is 0.7. These values combine to give 480 mm as an initial soil moisture content for SiB–GCM of which some 300 mm is available for evapotranspiration. This is twice the maximum water holding capacity (150 mm) of the soil hydrological models commonly used in GCMs, including Ctl–GCM, the UCLA/GLA GCM of Randall et al. (1985) and the GFDL GCM as described by Miyakoda and Sirutis (1986).

The partitioning of energy in the Sahara desert is simple and very similar in the two simulations. The total insolation in both GCMs decreases from 295 to 280 W m^{-2} over the course of the 50-day run due to the decrease in the solar inclination. The net solar radiation is 217 W m^{-2} in Ctl–GCM and 202 W m^{-2} in SiB–GCM; the 15 W m^{-2} difference is due to the difference in surface albedo which is 31% in SiB–GCM and 25% in Ctl–GCM. However, this difference in the net solar radiation is approximately compensated by differences in the net terrestrial radiation loss so the resulting net radiation is almost the same; 125 W m^{-2} in Ctl–GCM and 119 W m^{-2} in SiB–GCM. It is interesting to note that the net radiation in this region comprises only 40–45% of the incoming solar radiation as opposed to 70%–80% for the Amazon basin and the United States; this is due to the high surface albedo, high daytime soil surface temperature and low atmospheric humidity in the desert regions. Both models give very low evapotranspiration rates in this area so almost all the net radiation is returned to the atmosphere as sensible heat flux.

The calculated energy budgets for the Asian region are shown in Table 1. The differences between the two simulations are small because a large proportion of the region is desertic.

2) HYDROLOGICAL CYCLE

The simulated hydrological balance of the Amazon basin is shown in Figs. 8a and b. The precipitation rate is 6 mm day^{-1} in SiB–GCM and 7 mm day^{-1} in Ctl–GCM: the 1 mm day^{-1} decrease in the SiB–GCM versus the Ctl–GCM precipitation rate corresponds to the reduction in the SiB–GCM evaporation rate. The northern half of the Amazon basin is wet and the southern half is dry in summer, according to the climatological precipitation chart (Fig. F2d) of Jaeger (1976). If an area average is taken, we get 4–5 mm day^{-1} for the climatological rainfall rate in June–July for the entire Amazon basin. Compared with this observed value, both GCMs, especially Ctl–GCM, give more precipitation.

From Figs. 8a and 8b, we see that the precipitation exceeds evaporation by 1.5 mm day^{-1} on the average, with the difference made up by large-scale horizontal moisture convergence. This advected moisture contributes about 25% (SiB–GCM) and 20% (Ctl–GCM) to the total rainfall in the region.

The runoff rate in SiB–GCM is 2.5 mm day^{-1} on the average. This amount exceeds the difference between the rainfall and evaporation rates by 1 mm day^{-1} and implies that the total soil moisture content in SiB is steadily decreasing (see Fig. 9a). Oltman et al. (1964) estimated the annual mean outflow from the Amazon basin to be about 2.5 mm day^{-1} from observations of the Amazon River velocity profile and stage. There is a fairly considerable annual variation in this quantity, but the June to August period appears to bracket this mean value while showing a steadily decreasing outflow rate. This decrease in the outflow is consistent with a

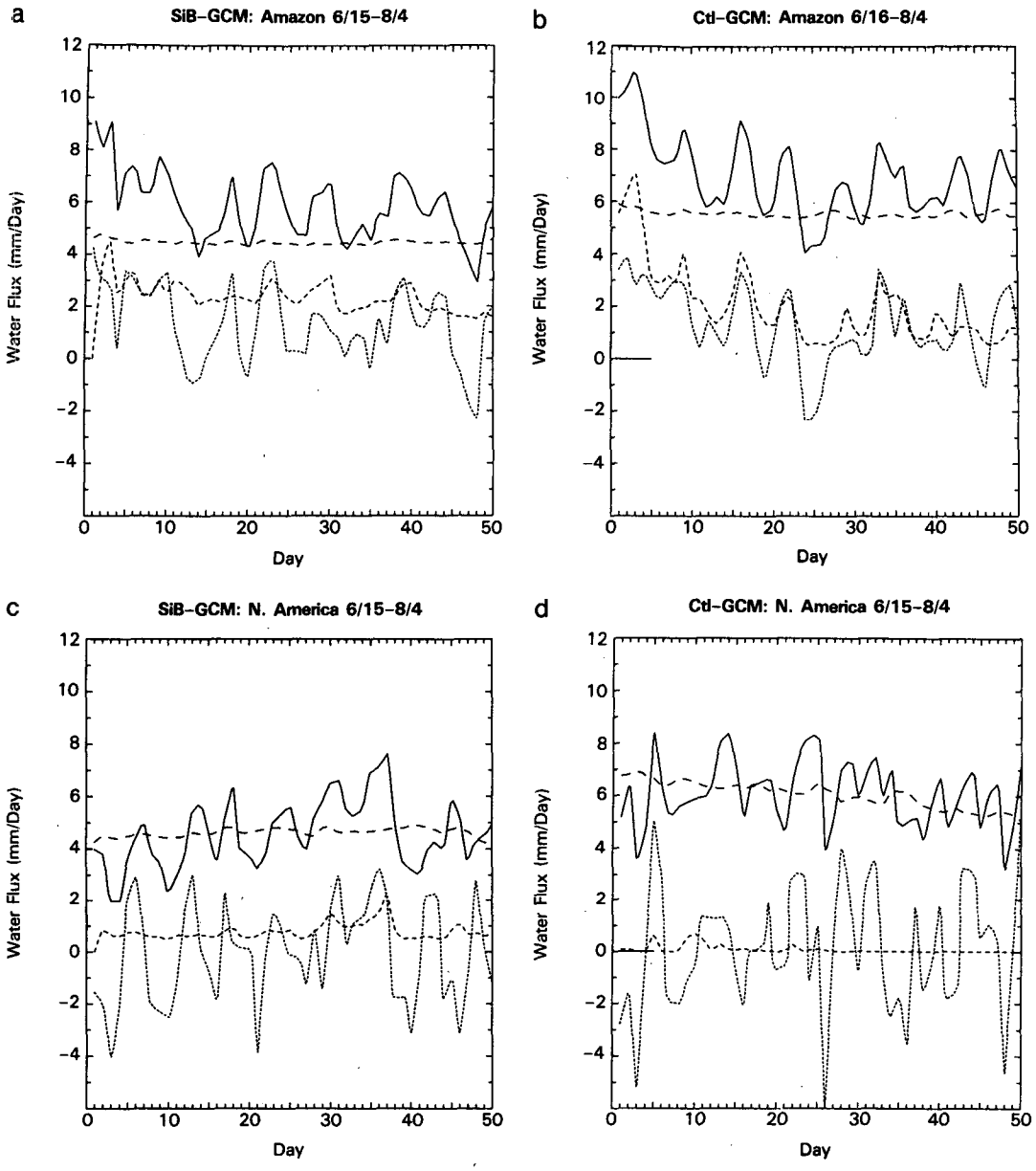

FIG. 8. (a) The daily mean moisture budget calculated by SiB–GCM in the Amazon basin for the 50-day (15 June–4 August) summer simulation run. The solid line is for precipitation, the coarse dashed line is for evaporation, the fine dashed line is for runoff and the dotted line is for horizontal moisture convergence in the atmosphere. All values are in mm day^{-1}. (b) As in Fig. 8a, but for Ctl–GCM. (c) As in Fig. 8a, but for central and eastern United States. (d) As in Fig. 8c, but for Ctl–GCM. (e) As in Fig. 8a, but for Asia. (f) As in Fig. 8e, but for Ctl–GCM. (g) The daily mean moisture budget as calculated by SiB–GCM for 30 days (15 June–14 July) in the eastern and central U.S. where the initial soil wetness was limited to a maximum of 0.45. Other conditions and symbols are the same as for the 50-day (15 June–4 August) summer SiB–GCM simulation. The legend is reproduced on the facing page.

fall in the average soil moisture content for the basin as calculated by SiB–GCM.

In Ctl–GCM, runoff is generated by the difference between rainfall and evaporation when the soil is saturated. When soil moisture was predicted (see below) it decreased significantly, but because soil moisture in the main Ctl–GCM run was interpolated from monthly climatology, the soil wetness in the Amazon basin was almost always at the saturated value, see Fig. 9b.

The moisture budget for the U.S. region is presented in Figs. 8c and 8d. In SiB–GCM (Ctl–GCM) the calculated precipitation rate is 4.7 mm day^{-1} (6.2 mm day^{-1}) and the evaporation rate is 4.5 mm day^{-1} (6.0 mm day^{-1}). In both cases, the time-mean of the hor-

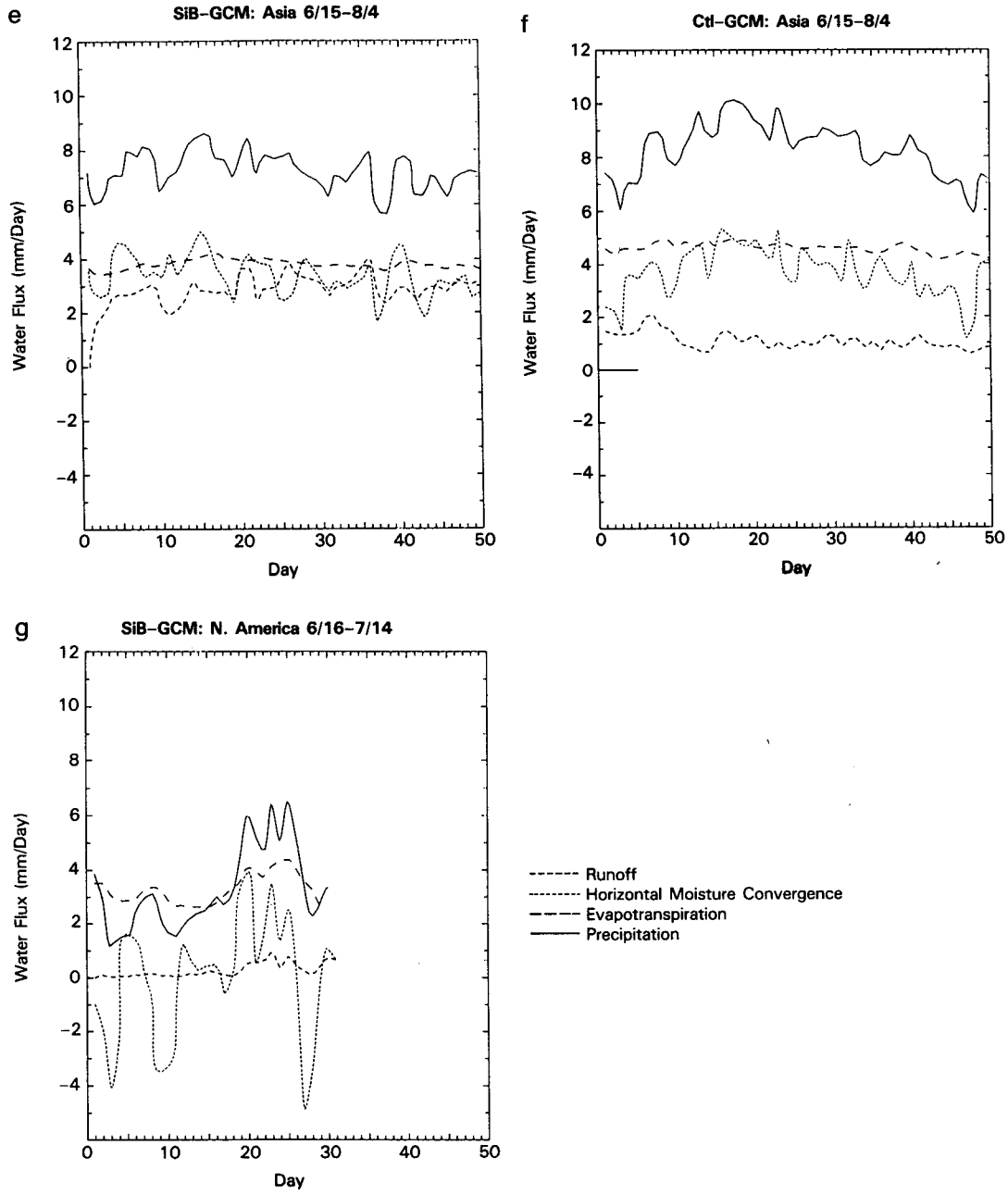

FIG. 8. (*Continued*)

izontal convergence of moisture by the large scale atmospheric circulation is very small. This result may be compared with the analysis of Rasmusson (1968) who computed the horizontal moisture convergence over the same central and eastern U.S. region for each month of the year from five years of radiosonde data. He estimated the surface evaporation rates to be 2.7 and 3.1 mm day^{-1} in June and July, respectively, and the horizontal convergence to be very slightly negative for both months. The evapotranspiration rate obtained from our simulation exceeds the estimates of Rasmusson (1968) by 50% in SiB–GCM and by 100% in Ctl–GCM. The corresponding evapotranspiration rate of 4.5 mm day^{-1} in SiB–GCM seems close to the values observed for a forest without soil moisture stress: 5 mm day^{-1} is given by Swift (1975) as the June–July mean for a deciduous forest in the southern Appalachians and 4 mm day^{-1} is given by Luxmoore (1983) as the July–September mean for a deciduous forest in the eastern United States.

From the hydrological analyses of the Amazon and central and eastern U.S. regions, we note that the higher precipitation rates over land in Ctl–GCM were associated with higher evapotranspiration rates over the same area and not from an increase in horizontal moisture convergence. This leads us to suggest that the precipitation over these regions is in large part controlled by the transpiration there. In order to check this hypothesis, another SiB–GCM experiment was performed with a reduced initial soil moisture content.

A 30-day SiB–GCM run was performed using the same initial conditions as the 50-day summer SiB–GCM run except that in North America the initial soil wetness was set to 0.45 wherever it exceeded this value. Figure 8g shows the moisture budget for the central and eastern U.S. region as calculated for this run. Once again, the time-averaged horizontal moisture convergence is almost zero and the reduced evapotranspiration rate, down from 4.5 mm day^{-1} in the original 50-day SiB–GCM run to less than 3.5 mm day^{-1} in this reduced soil moisture case, is reflected by a corresponding 1 mm day^{-1} decrease in the time-averaged precipitation rate. This result strongly supports the hypothesis that the evapotranspiration and rainfall rates are tightly coupled in this region during the summer months.

Returning to the original summer run, the runoff generated for the U.S. region by SiB–GCM is 1 mm day^{-1} and is not in equilibrium with the precipitation rate minus the evaporation rate. As in the case of the Amazon basin, the runoff is generated from drainage from the recharge zone of the SiB soil moisture model.

The moisture budget for Asia in the summer run is shown in Figs. 8e and 8f. The precipitation rate in SiB–GCM (Ctl–GCM) is 7.2 mm day^{-1} (8.5 mm day^{-1}), evapotranspiration 3.8 mm day^{-1} (4.7 mm day^{-1}), horizontal moisture convergence 3.4 mm day^{-1} (3.8 mm day^{-1}) and runoff 3.0 mm day^{-1} (1.1 mm day^{-1}). The decrease in precipitation (1.3 mm day^{-1}) in SiB–GCM compared to Ctl–GCM comes partly from a decrease in the horizontal moisture convergence (0.4 mm day^{-1}). The main characteristic to note for this region is that horizontal convergence is calculated to make a significant contribution to the precipitation in both GCMs for this region. Because runoff is less than precipitation minus evaporation in SiB–GCM, the soil moisture in the region increases slowly from 0.45 to 0.50 during the run (Fig. 9a). At the same time the climatological soil moisture prescribed in Ctl–GCM increases from 0.43 to 0.54 (Fig. 9b).

We continuously updated the soil moisture content in the Ctl–GCM to conform to the climatological estimates of Willmott et al. (1985). An additional 30-day Ctl–GCM run was performed in which the soil moisture was predicted by the model. Figure 9c shows the predicted time evolution of soil moisture which may be directly compared with Fig. 9b. It may be seen that the predicted soil moisture decreases more rapidly in the Amazon region, but more slowly in the central and eastern U.S. as compared with the imposed climatology.

In Figs. 9b and 9c, the differences between the simulated and climatological time-series of soil moisture are due to regional differences in the precipitation–evaporation ratios as simulated by Ctl–GCM and calculated by Willmott et al. (1985). However, the difference in the wetness values associated with the prognostic and climatological soil moisture fields was comparatively small and so the difference between the global fields of evapotranspiration and sensible heat flux produced by the two Ctl–GCM runs was slight; at day 30, the version with the predicted soil moisture gave rise to a sensible heat flux of only 10 W m^{-2} less over the United States than that obtained with the climatological soil moisture field. There was virtually no difference in the heat flux fields calculated for the Amazon by the two Ctl–GCM runs at this time.

c. Global surface field

1) SUMMER CASE

The surface latent heat flux for the first 30 days of the summer simulation by SiB–GCM (Ctl–GCM) is shown in Fig. 10a (10b) and the difference in Fig. 10c. Except for the deserts, the latent heat flux in Ctl–GCM over the continents is usually more than 150 W m^{-2} and sometimes exceeds 200 W m^{-2} in parts of North America and South Asia. In SiB–GCM, latent heat fluxes of more than 150 W m^{-2} are observed only in South Asia. The difference map shows that SiB–GCM gives 25–50 W m^{-2} (1–2 mm day^{-1}) less evapotranspiration over most vegetated land.

We compared the latent heat flux calculated with SiB–GCM with the global map of climatological latent heat flux for June as estimated by Budyko (1974). Budyko's estimates were found to be less than the simulated value over all land surfaces. For example, his estimated latent heat fluxes in the Amazon basin and central/eastern United States are 80 and 60 W m^{-2}, respectively, which are much less than the observed values of 90–120 and 90 W m^{-2} for the respective regions cited in the previous subsection. The global map of surface net radiation (Budyko 1974) shows values which were typically one half of the downward solar radiation over the land surface. The simulations from both GCMs suggest that this only happens over deserts where both the surface albedo and the daytime surface temperatures are high and the atmospheric humidity is low and that over densely vegetated regions like the Amazon basin only about 30% of the insolation is reflected or re-emitted: see Table 1. Although the net loss of surface energy by terrestrial radiation is dependent on the amount and height of the prescribed cloud in both the climatological estimation (Budyko 1974) and the GCMs, Budyko's value seems to underestimate the

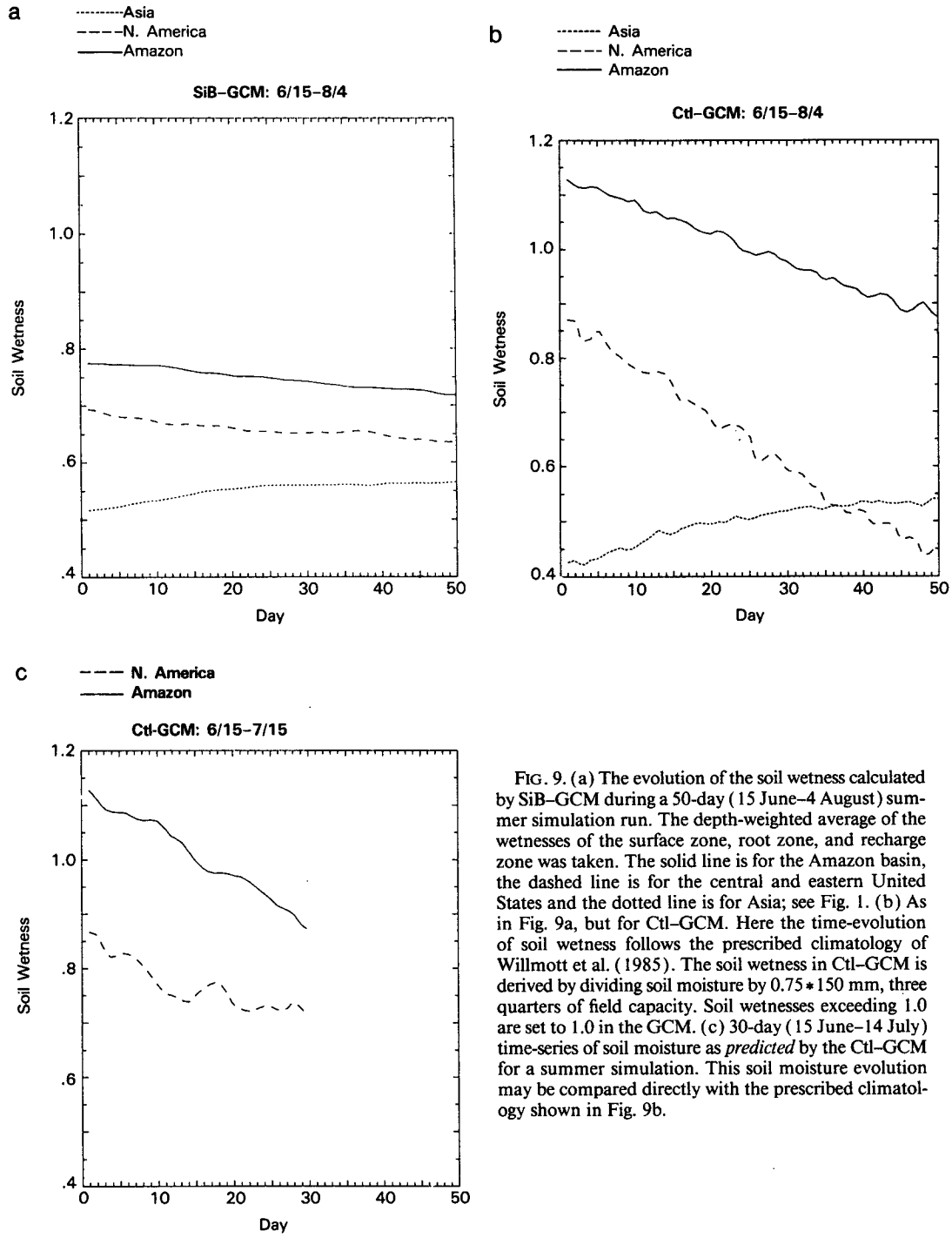

FIG. 9. (a) The evolution of the soil wetness calculated by SiB–GCM during a 50-day (15 June–4 August) summer simulation run. The depth-weighted average of the wetnesses of the surface zone, root zone, and recharge zone was taken. The solid line is for the Amazon basin, the dashed line is for the central and eastern United States and the dotted line is for Asia; see Fig. 1. (b) As in Fig. 9a, but for Ctl–GCM. Here the time-evolution of soil wetness follows the prescribed climatology of Willmott et al. (1985). The soil wetness in Ctl–GCM is derived by dividing soil moisture by 0.75 * 150 mm, three quarters of field capacity. Soil wetnesses exceeding 1.0 are set to 1.0 in the GCM. (c) 30-day (15 June–14 July) time-series of soil moisture as *predicted* by the Ctl–GCM for a summer simulation. This soil moisture evolution may be compared directly with the prescribed climatology shown in Fig. 9b.

net radiation and consequently the latent and sensible heat fluxes.

Figures 11a and 11b show the mean daily precipitation rate simulated by SiB–GCM (Ctl–GCM) and Fig. 11c the difference between them. For comparison, a climatological field for the June–July period (Jaeger 1976) is presented in Fig. 11d. Generally, the simulated precipitation pattern agrees well with the climatology, but the Ctl–GCM field is marked by much higher precipitation rates in North America and northern Eurasia. There is also a northward shift of the monsoon rainbelt in Asia in SiB–GCM relative to Ctl–GCM.

The difference map, Fig. 11c, clearly illustrates the reduction in precipitation over vegetated land due to

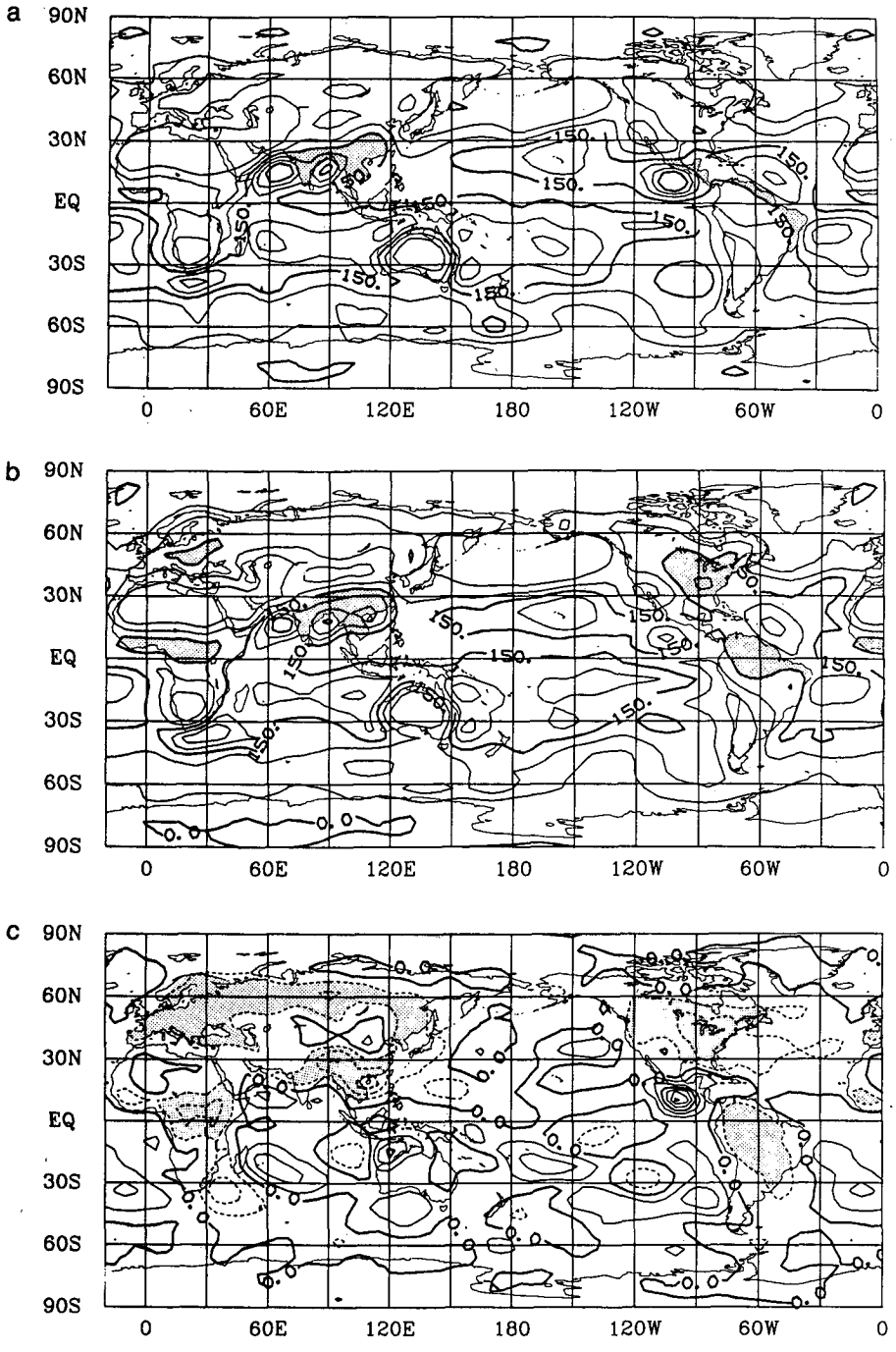

FIG. 10. (a) Global field of mean surface latent heat flux in the SiB–GCM summer simulation for the first 30-day period (15 June–14 July). The contour interval is 50 W m^2. Land areas with mean latent heat fluxes in excess of 150 W m^{-2} have been shaded. (b) As in Fig. 10a, but for Ctl–GCM. (c) The difference between the 30-day (15 June–14 July) mean latent heat fluxes of the summer simulations: SiB–GCM minus Ctl–GCM. The contour interval is 25 W m^{-2}. The land areas where Ctl–GCM produces >25 W m^{-2} of latent heat flux compared to SiB–GCM have been shaded.

SiB–GCM. In parts of North America and Eurasia, the precipitation difference exceeds 2 mm day^{-1} which amounts to a SiB–GCM reduction of 25%–50% from the Ctl–GCM precipitation; in the Amazon basin, the reduction is about 25%. This dramatic decrease in precipitation over the land in SiB–GCM brings the cal-

culated precipitation closer to the climatology (see Fig. 11d), but in many areas, notably North America and northern Brazil, the precipitation rate calculated by SiB–GCM is still 1–2 mm day^{-1} higher than the climatology.

The surface sensible heat flux for the first 30 days in the summer simulation by SiB–GCM (Ctl–GCM) is shown in Fig. 12a (12b) with the difference shown in Fig. 12c. The time-averaged sensible heat flux calculated by SiB–GCM is always greater than that calculated by Ctl–GCM over the vegetated land. The negative value observed in the difference field in northern China is a result of the greater soil wetness calculated by SiB–GCM for this region, the wetter soil being due to the northward shift of the rainbelt in China in SiB–GCM.

Figures 13a and 13b show the daytime PBL depth as simulated by SiB–GCM (Ctl–GCM). The PBL depth was derived by counting the number of layers where the 30-day mean heating rate generated by vertical diffusion exceeded 1°K day^{-1}. This definition was found to agree well with the conventional method of using potential temperature gradients. Except for the deserts, the PBL depth in Ctl–GCM was calculated to be about 20 mb over the land which is unrealistically shallow; this is a direct result of the small sensible heat flux generated by Ctl–GCM. In SiB–GCM the PBL depth is more than 60 mb over most of the vegetated land and in the Amazon basin, the simulated depth of 100 mb agrees well with the observations of Martin et al. (1988). In both GCMs the PBL grew to 300 mb at some desert grid points. This very high value is consistent with the report of Blake et al. (1983) that the PBL depth in the Saudi Arabian desert could reach 350 mb.

Because the daytime PBL in the SiB–GCM simulation is more unstable than that of Ctl–GCM, momentum transport is more efficient in the former model. This results in a larger surface wind stress in SiB–GCM over land. The values over the oceans are almost the same for both GCMs and agree fairly well with those estimated from surface data by Hellerman and Rosenstein (1983), but over the continents, the SiB–GCM value is almost twice as large as the Ctl–GCM value.

2) WINTER CASE

In the winter simulation, the two 30-day (15 December–13 January) runs were made with the surface drag parameterization of Deardorff (1972) which gave a slightly larger surface drag for stable and neutral conditions than the formulation based on the Monin–Obukhov model used in the summer simulations. This different formulation tended to reduce the Bowen ratio slightly but the overall difference between the two GCMs was the same as in the summer simulation.

Figures 14, 15, and 16 show the differences between the latent heat flux, sensible heat flux and precipitation 30-day mean fields as calculated by SiB–GCM and Ctl–GCM for the 30-day winter simulation. The SiB–GCM enhances sensible heat flux over vegetated land areas. The reduced sensible heat flux over Australia calculated by SiB–GCM is associated with higher desert albedo values relative to the Ctl–GCM prescription.

The simulated precipitation patterns from both GCMs are in good agreement with the climatology except in the Amazon basin. The climatological precipitation field exhibits one local maximum in the Amazon basin but the simulated precipitation fields have two local maxima in the region, one in the northeast and another in the southeast of Brazil. SiB–GCM is associated with decreased precipitation over land (through the reduction of evapotranspiration) but SiB did not change the basic precipitation pattern; it seems that other physics parameterizations in the GCM may be responsible for this result.

These winter case difference fields, Figs. 14, 15 and 16, should be directly compared with their summer case counterparts, Figs. 10c, 11c and 12c, respectively. It is clear that the largest differences between the SiB–GCM and Ctl–GCM energy and water budgets are associated with the humid vegetated regions during the growing season. For example, the North American and Eurasian continents exhibit coherent differences in all three fields for the summer simulations, but relatively weak differences during the winter and an opposite but weaker trend can be seen for South America. This is to be expected as the growing season is associated with high radiation loads and significant biophysical control of evapotranspiration. The first factor leads to strong evaporative demands in both models, but only SiB–GCM includes a description of stomatal resistance, which greatly reduces the calculated evapotranspiration and hence the precipitation.

d. Impact on the large-scale atmospheric circulation

The shortness of the simulation runs performed with SiB–GCM and Ctl–GCM and the uncertainties in the soil moisture initialization prevent us from drawing definitive conclusions about the impact of SiB on the large-scale atmospheric circulation. Longer runs, where the effects of the soil moisture initialization scheme can be disregarded, must be carried out to fully investigate the interactions between the surface energy balance and the large-scale circulation.

1) SUMMER CASE

In SiB–GCM, the tropospheric jet in the Northern Hemisphere was weaker than that simulated by Ctl–GCM. Wind speeds of more than 30 m s^{-1} were observed in the NMC analysis and in the Ctl–GCM simulated field but not in the SiB–GCM simulated field. The jet stream was also shifted slightly northward in the SiB–GCM simulation. The enhanced drag force

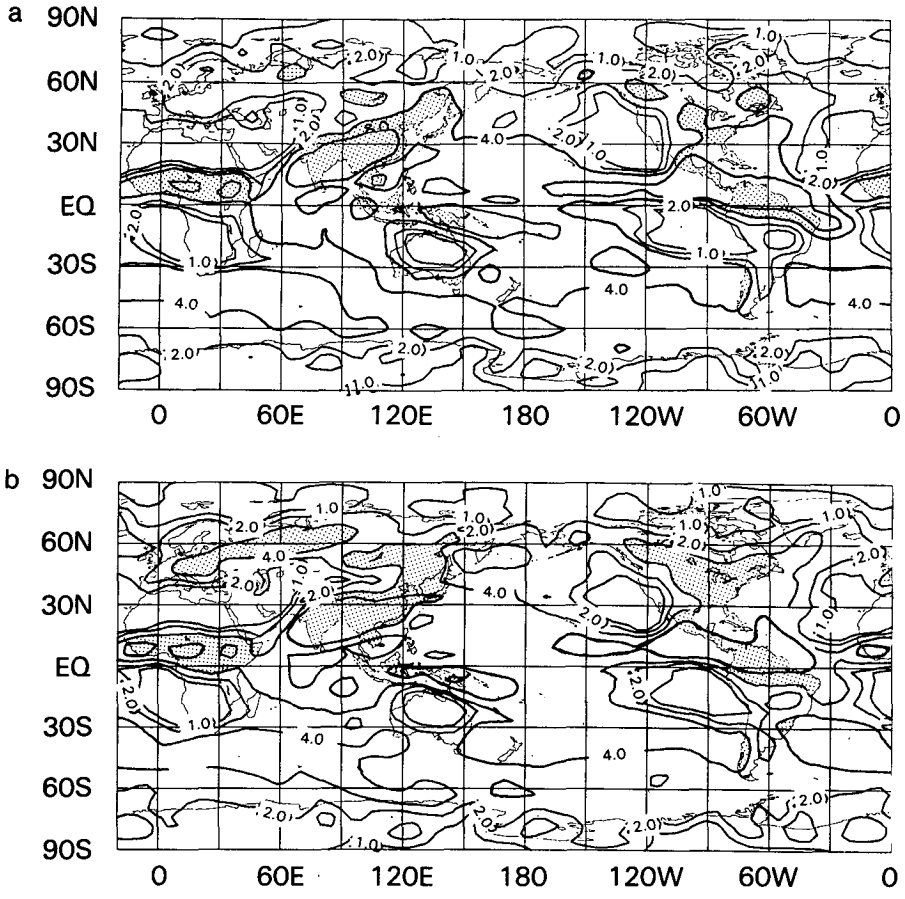

FIG. 11. (a) Mean daily total (convective and large scale) precipitation in the SiB–GCM summer simulations for the first 30-day (15 June–14 July) period. The contour intervals are 1.0, 2.0, 4.0, and 8.0 mm day^{-1}. Land areas with rainfall rates greater than 4.0 mm day^{-1} have been shaded. (b) As in Fig. 11a, but for Ctl–GCM. (c) The difference between the 30-day (15 July–14 July) mean daily precipitation rates for the summer simulations: SiB–GCM minus Ctl–GCM. The contour interval is 1 mm day^{-1}. The land areas where Ctl–GCM produces >1 mm day^{-1} of precipitation compared to SiB–GCM have been shaded. (d) Mean observed daily precipitation for June–July from Jaeger (1976). Contours and shading correspond to Figs. 11a and 11b.

over land discussed in section 4c(1) may have some implications for the deceleration of tropospheric jets.

There was little difference between the fields of the 500-mb eddy geopotential height for the first 30 days of the summer simulation as simulated by SiB–GCM and Ctl–GCM. When compared with the NMC analysis, the simulations by both GCMs appear to be better in the Northern rather than the Southern Hemisphere. The wavy pattern over the Eurasian continent in the SiB–GCM simulation is flatter than in the Ctl–GCM simulation while the trough to the north of the Caspian Sea is completely missed in the SiB–GCM simulation: see Sato et al. (1989).

2) WINTER CASE

The simulation of the circulation in the Northern Hemisphere is very good in both GCMs when compared with the analyzed field. Ctl–GCM simulates the ridge around Lake Baikal better than SiB–GCM, but the ridge to the south of New Zealand seems to be better represented in SiB–GCM: see Sato et al. (1989).

5. Summary and discussion

The Simple Biosphere Model (SiB) developed by Sellers et al. (1986) was implemented in a modified version of the NMC spectral model. The SiB–GCM was integrated for 50 days in a (boreal) summer simulation and for 30 days in a (boreal) winter simulation. The simulated surface and atmospheric fields were compared with those produced by the control GCM (Ctl–GCM) which has the same physical parameterization as SiB–GCM except for the "bucket" hydrological model and the three soil layers with predicted temperatures.

The Ctl–GCM was found to give too much evaporation over the vegetated land; sometimes the latent

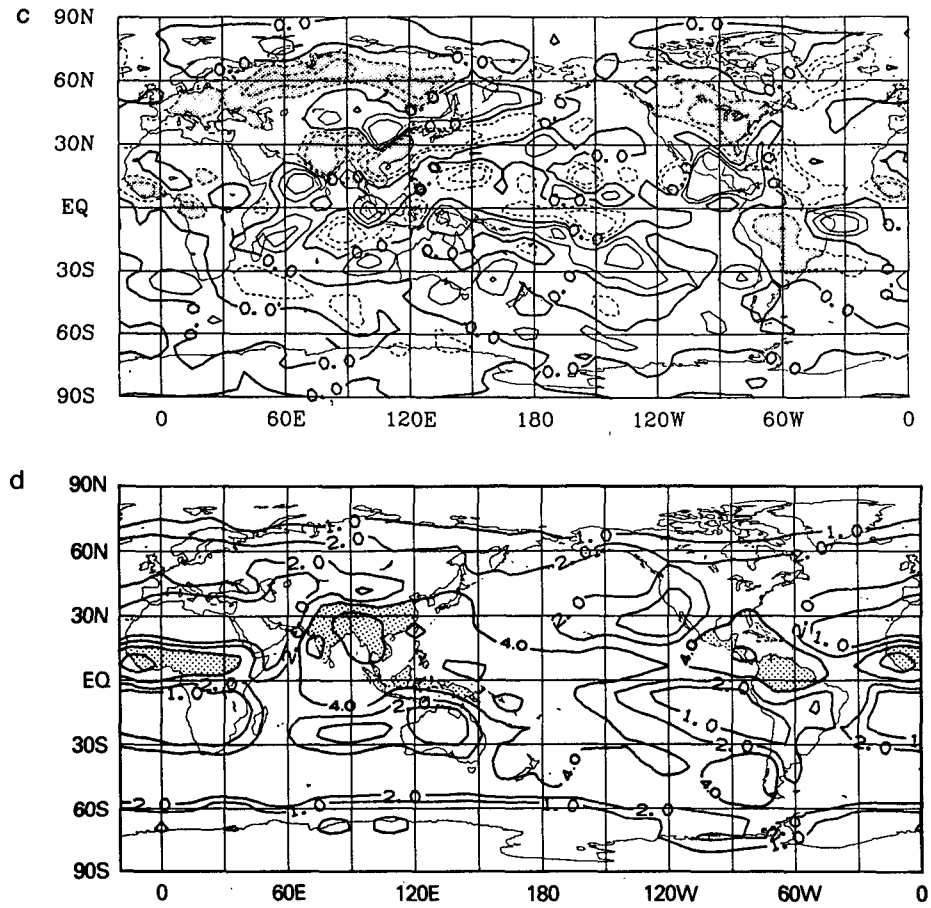

FIG. 11. (*Continued*)

heat flux was almost equal to the net radiation. On the other hand, SiB–GCM generated sensible and latent fluxes over the land which compared well with observations. The improvement in the calculated Bowen ratio in SiB–GCM comes mainly from the explicit treatment of the biophysical control of transpiration by the vegetation stomatal resistance.

There is a secondary effect due to the generally higher land-surface albedos calculated by SiB–GCM as compared to the prescribed fields used in Ctl–GCM. This is thought to alter the total available energy by about 6% in vegetated areas with a similar impact on the evapotranspiration rate. The stomatal resistance effect, however, accounts for the rest of the reduction in evapotranspiration, typically 25% or greater over the moist vegetated regions. This result corresponds with those in the sensitivity study of Sellers and Dorman (1987).

The increase in the sensible heat flux (25–50 W m^{-2}) over the vegetated land calculated by SiB–GCM was associated with higher surface temperatures and larger and more realistic diurnal ranges in the surface and PBL temperatures. The daytime PBL depth was 60–100 mb over vegetated land in SiB–GCM. A deeper PBL and more active momentum exchange over the land led to an increase in the surface stress calculated by SiB–GCM.

The SiB–GCM June–July precipitation rate was 1 to 2 mm day^{-1} lower than in the Ctl–GCM run in the Amazon basin, the African tropics, North America, the Soviet Union and Europe. The monsoon rainbelt in China moved northward, but overall the precipitation there also decreased. This difference in the precipitation rates corresponded roughly to the difference in the time-averaged latent heat fluxes, i.e., about 25–50 W m^{-2}.

The SiB–GCM still generated more rain than the given climatological precipitation in some places over land. This may be due to inadequacies in the physical parameterizations in the GCM or insufficient sampling. Alternatively, it could be that SiB–GCM still calculates evapotranspiration rates that are too high because of problems in the soil moisture initialization. Over the central and eastern United States, the simulated horizontal moisture convergence in June–July was almost zero in both GCMs, in agreement with observations,

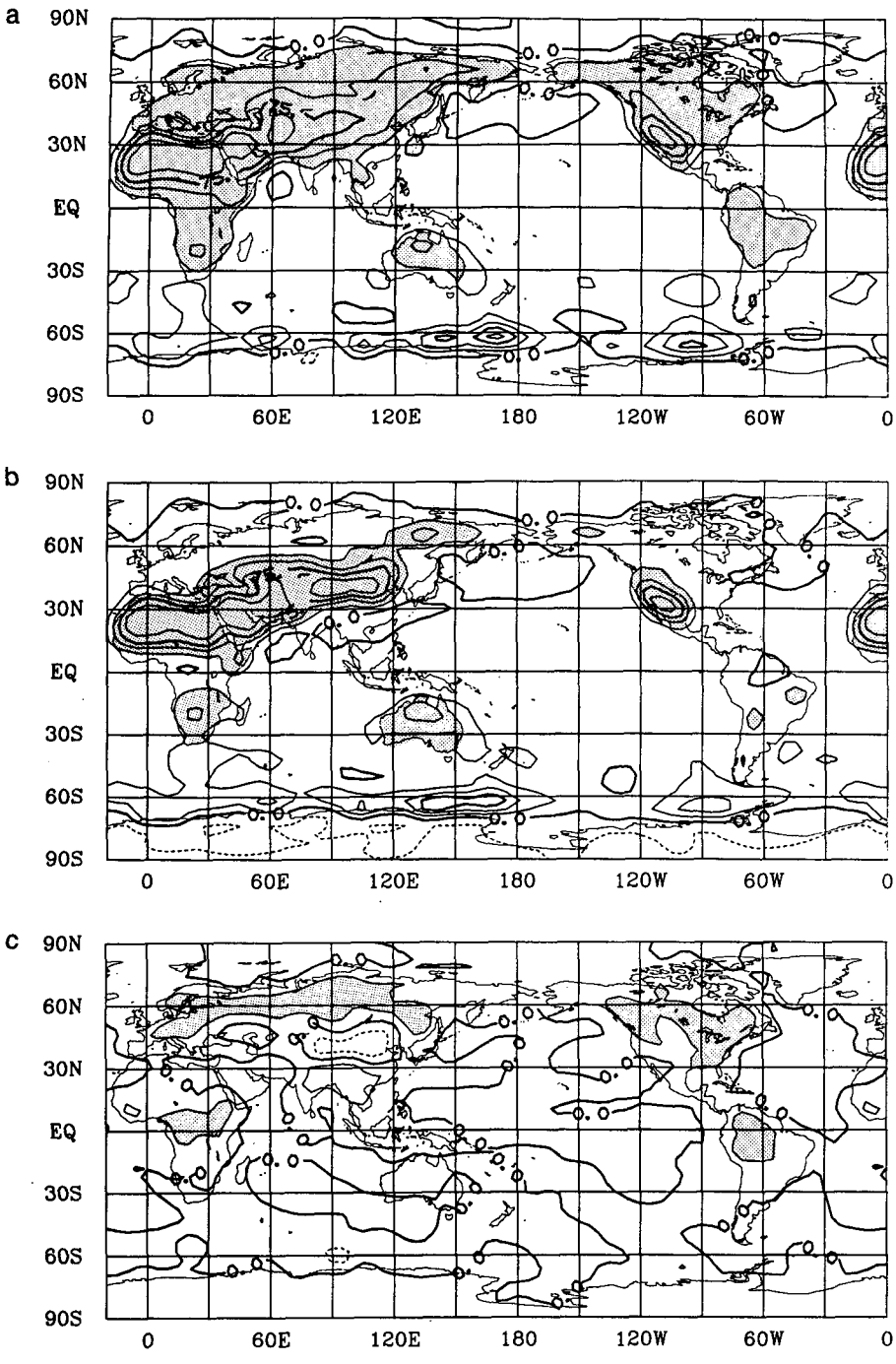

FIG. 12. (a) Global field of the mean surface sensible heat flux in the SiB–GCM summer simulation for the first 30-day period (15 June–14 July). The contour interval is 25 W m^{-2}. Land areas with mean sensible heat fluxes in excess of 25 W m^{-2} have been shaded. (b) As in Fig. 12a, but for Ctl–GCM. (c) The difference of 30-day (15 June–14 July) mean sensible heat fluxes for the summer simulations: SiB–GCM minus Ctl–GCM. The contour interval is 25 W m^{-2}. Land areas where SiB–GCM produces >25 W m^{-2} of sensible heat flux compared to Ctl–GCM have been shaded.

but the evaporation rate and hence the precipitation rate in the region was far lower in SiB–GCM. This suggests that the excessive precipitation calculated over land by Ctl–GCM may in large part be the result of an overestimation of the surface evaporation rate. An experiment was performed to explore this hypothesis by

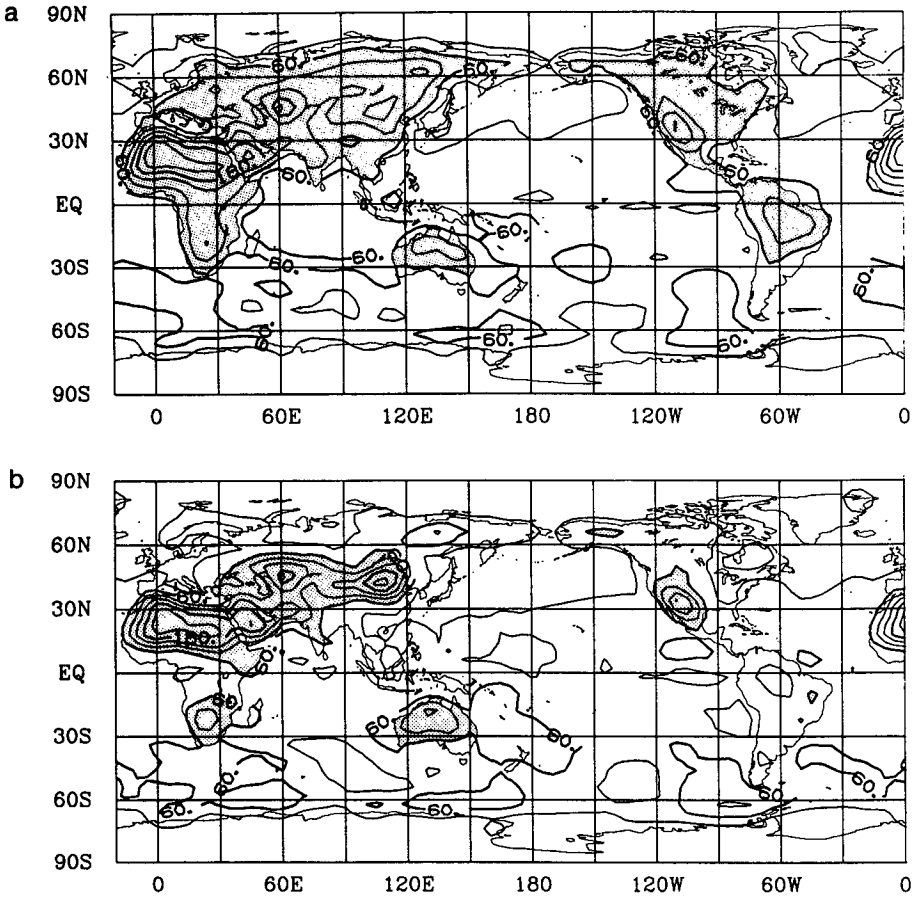

FIG. 13. (a) Mean maximum PBL height in the SiB–GCM summer simulation for the 30-day (15 June–14 July) period. The contour interval is 30 mb. Land areas where the mean maximum PBL height exceeds 60 mb have been shaded. (b) As in Fig. 13a, but for Ctl–GCM.

integrating SiB–GCM with a lower initial soil moisture in central and eastern United States. The results showed that the simulated horizontal moisture convergence remained almost zero while the smaller evapotranspiration rate over land directly contributed to a reduction in the precipitation rate.

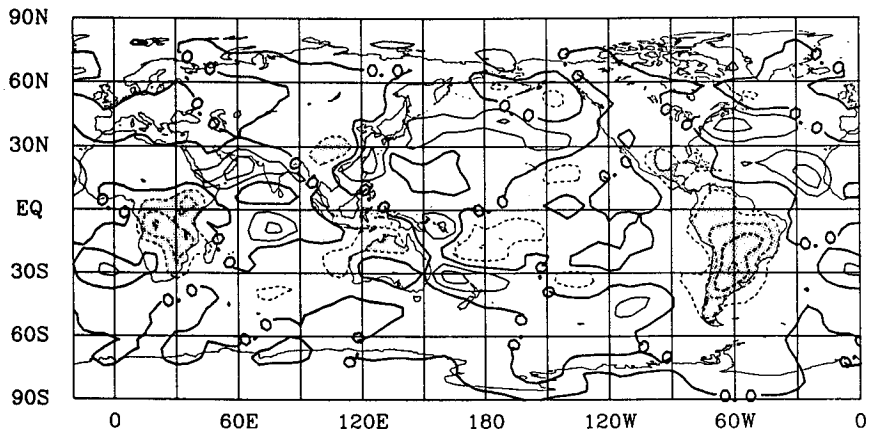

FIG. 14. Difference field of latent heat flux as calculated by SiB–GCM and Ctl–GCM for 30-day (15 December–13 January) winter simulations: SiB–GCM minus Ctl–GCM. The contour interval is 25 W m^{-2}. Land areas where Ctl–GCM produces >25 W m^{-2} of latent heat flux compared to SiB–GCM have been shaded.

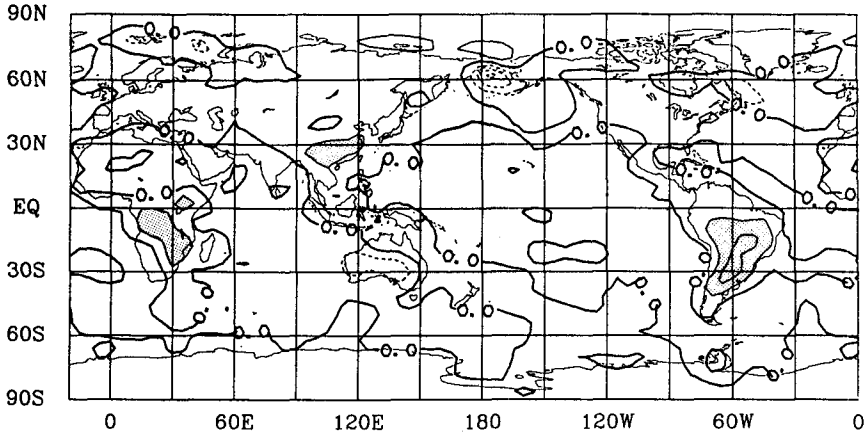

FIG. 15. Difference field of sensible heat flux as calculated by SiB–GCM and Ctl–GCM for the 30-day (15 December–13 January) winter simulations: SiB–GCM minus Ctl–GCM. The contour interval is 25 W m^{-2}. Land areas where SiB-GCM produces more than 25 W m^{-2} of sensible heat flux than Ctl–GCM have been shaded.

In the course of the 50-day simulation, soil wetness in SiB–GCM changed very slowly. This was partly due to the large soil moisture capacity in the SiB formulation and partly due to the small differences between evapotranspiration and precipitation.

In Ctl–GCM, soil wetness was updated every day from values interpolated from monthly climatology. Over vegetated land in the Northern Hemisphere the soil moisture decreased rapidly over the June–August period. This brought about a gradual increase in the sensible heat flux and a decrease in the latent heat flux which in turn led to a reduced precipitation rate.

The realism of SiB–GCM and Ctl–GCM on smaller spatial scales was also scrutinized. The diurnal variation and the mean value of the albedo as calculated with SiB–GCM were found to be satisfactory when compared with observations while the albedos used in Ctl–GCM were generally too low. The calculated interception loss fraction is difficult to verify, but at least in the Amazon basin the SiB–GCM value of 28% of the total latent heat flux seems to be reasonable. Overall, SiB–GCM appears to give a more consistent and realistic simulation of hydrological processes and near-surface atmospheric conditions than Ctl–GCM.

It should also be noted that the differences between the values of sensible heat flux, evapotranspiration and precipitation calculated by the two models are maximized in the humid vegetated regions of the summer (growing season) hemisphere. Under the prevailing conditions of low relative humidity and high radiation loads the evaporation rate is very sensitive to the value of the stomatal resistance, which is around 100 s m^{-1} in SiB–GCM and effectively zero in Ctl–GCM.

A preliminary assessment of the impact of SiB on

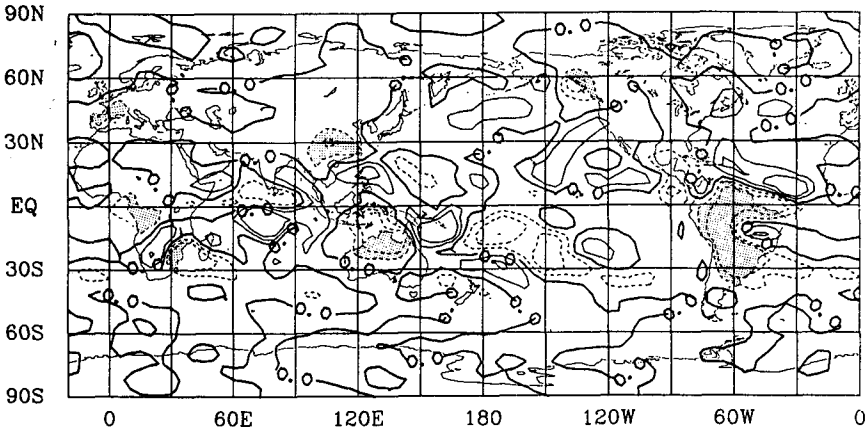

FIG. 16. Difference field of mean daily precipitation rate (large-scale plus convective) as calculated by SiB–GCM and Ctl–GCM for the 30-day (15 December–13 January) winter simulations: SiB–GCM minus Ctl–GCM. The contour interval is 1 mm day^{-1}. Land areas where Ctl–GCM produces more than 1 mm day^{-1} of precipitation than SiB–GCM have been shaded.

the large-scale atmospheric circulation was also made. The large-scale circulation changed only slightly in the Northern Hemisphere winter simulation. This is understandable because of the small land area in the Southern Hemisphere and because the continents in the Northern Hemisphere receive little solar radiation in winter.

In the summer simulation there was some noticeable impact: the 200 mb jet stream was found to be unfavorably weakened in SiB–GCM which also failed to simulate the stationary trough in the 500 mb geopotential height. We do not yet understand the causality of this effect. Clearly, the above comments must be regarded as very preliminary in view of the shortness of the simulation runs (50 days or less) and the uncertainties in the soil moisture initialization.

In summary, the implementation of SiB in the GCM has improved the simulated partition of absorbed energy at the land surface. Generally, the explicit recognition of stomatal resistance in the SiB latent heat flux formulation has resulted in a reduction in the land surface evapotranspiration rate compared to the bucket model calculation. In the summer hemisphere, this led to approximately matching reductions in the continental precipitation rates and increases in the diurnal amplitude of the PBL and surface air temperatures in SiB–GCM. The reductions in evapotranspiration and rainfall rates over the land due to SiB seem to be supported by observations.

Acknowledgments. The first author is grateful to the Japan Meteorological Agency and COLA (University of Maryland) for facilitating his visit to the University of Maryland. Thanks are also extended to Dr. Harshvardhan and Tom Corsetti for help with some of the radiation code, to Jeff Dorman and Larry Marx for organizing the SiB vegetation parameter sets, and to Dr. Jim Shuttleworth for providing some of the detailed Amazon tropical forest data. This research was supported by NSF Grant ATM-8414660, NASA Grants NAG5-492, NAGW-1269, and NAGW-557. Special thanks go to Marlene Schlichtig for typing and proofreading many drafts of the manuscript.

REFERENCES

Blake, D. W., T. N. Krishnamurti, S. V. Low-Nam and J. S. Fein, 1983: Heat low over the Saudi Arabian desert during may 1979 (Summer MONEX). *Mon. Wea. Rev.*, **111**, 1759–1774.

Budyko, M. I., 1974: *Climate and Life.* Academic Press, 508 pp.

Carson, D. J., and A. B. Sangster, 1981: The influence of land-surface albedo and soil moisture on general circulation model simulations. *Numerical Experimentation Programme Report.* No. 2, 5.14–5.21.

Charney, J. G., W. J. Quirk, S. H. Chow and J. Kornfield, 1977: A comparative study of the effects of albedo change on drought in semi-arid regions. *J. Atmos. Sci.*, **34**, 1366–1385.

Chervin, R. M., 1979: Response of the NCAR general circulation model to changed land surface albedo. *Report of the JOC Study Conference on Climate Models: Performance, Intercomparison and Sensitivity Studies, Vol. I,* 563–581.

Davies, R., 1982: Documentation of the solar radiation parameterization in the GLAS Climate Model. NASA Tech. Memo. 83961, p. 57.

Deardorff, J. W., 1972: Parameterization of the planetary boundary layer for use in General Circulation Models. *Mon. Wea. Rev.*, **100**, 93–106.

——, 1977: Efficient prediction of ground surface temperature and moisture with inclusion of a layer of vegetation. *J. Geophys. Res.*, **83**, 1889–1903.

Dickinson, R. E., 1984: Modeling evapotranspiration for three-dimensional global climate models. *Climate Processes and Climate Sensitivity.* J. E. Hanson and T. Takahashi, Eds., *Geophys. Monogr.*, Amer. Geophys. Union, **29**, 58–72.

——, and A. Henderson-Sellers, 1988: Modelling tropical deforestation: A study of GCM land-surface parameterizations. *Quart. J. Roy. Meteor. Soc.*, **114**, 439–462.

Dorman, J. L., and P. J. Sellers, 1989: A global climatology of albedo, roughness length and stomatal resistance for atmospheric general circulation models as represented by the Simple Biosphere model (SiB). *J. Appl. Meteor.* in press.

Fels, S. B., and M. D. Schwarzkopf, 1975: The simplified exchange approximation: A new method for radiative transfer calculations. *J. Atmos. Sci.*, **32**, 1475–1488.

Franken, W., P. R. Leopoldo, E. Matsui and M. N. G. Ribeiro, 1982: Interceptacao das precipitacoes em floresta Amazonica de terra firme. *Acta Amazon*, **12**, 15–22.

Harshvardhan, and T. G. Corsetti, 1984: Longwave radiation parameterization for the UCLA/GLAS GCM. NASA Tech. Memo. 86072, p. 65.

——, R. Davies, D. A. Randall and T. G. Corsetti, 1987: A fast radiation parameterization for general circulation models. *J. Geophys. Res.*, **92**, 1009–1016.

Hellerman, S., and M. Rosenstein, 1983: Normal monthly wind stress over the world ocean with error estimates. *J. Phys. Oceanogr.*, **13**, 1093–1104.

Jaeger, L., 1976: Monatskarten des Niederschlages fur die ganze Erde. *Ber. Dtsch. Wetterdienst*, **18**(139).

Kinter III, J. L., J. Shukla, L. Marx and E. K. Schneider, 1988: A simulation of the winter and summer circulations with the NMC global spectral model. *J. Atmos. Sci.*, **45**, 2486–2522.

Kuo, H. L., 1965: On the formation and intensification of tropical cyclones through latent heat release by cumulus convection. *J. Atmos. Sci.*, **22**, 40–63.

Lacis, A. A., and J. E. Hansen, 1974: A parameterization for the absorption of solar radiation in the earth's atmosphere. *J. Atmos. Sci.*, **31**, 118–133.

Luxmoore, R. J., 1983: Water budget of an eastern deciduous forest stand. *Soil Sci. Soc. Am. J.*, **47**, 785–791.

Manabe, S., 1969: The atmospheric circulation and hydrology of the Earth's surface. *Mon. Wea. Rev.*, **97**, 739–774.

Martin, C. L., D. Fitzjarrald, M. Garstang, A. P. Oliveira, S. Greco and E. Browell, 1988: Structure and growth of the mixing layer over the Amazonian rain forest, *J. Geophys. Res.*, **(D2)**, 1361–1377.

Matthews, E., 1984: Global vegetation and land use: New high-resolution data bases for climate studies. *J. Clim. Appl. Meteor.*, **22**, 474–487.

McNaughton, K. G., and T. A. Black, 1973: A study of evapotranspiration from a Douglas fir forest using the energy balance approach. *Water Resour. Res.*, **9**, 1579–1590.

Mellor, G. L., and T. Yamada, 1982: Development of a turbulence closure model for geophysical fluid problems. *Rev. Geophys. Space Phys.*, **20**, 851–875.

Mintz, Y., 1984: The sensitivity of numerically simulated climates to land-surface conditions. *The Global Climate.* J. Houghton, Ed., Cambridge University Press, 79–105.

Miyakoda, K., and J. Sirutis, 1977: Comparative integrations of global spectral models with various parameterized processes of subgrid scale vertical transports. *Beitr. Phys. Atmos.*, **50**, 445–447.

——, and ——, 1986: Manual of E-physics. Manuscript, GFDL, Princeton, New Jersey.

Monteith, J. L., 1973: *Principles of Environmental Physics.* Edward Arnold, 242 pp.

Oltman, R. E., H. O. R. Sternbert, F. C. Ames and L. C. Davis, Jr., 1964: Amazon River investigations reconnaissance measurements of July. *U.S. Geol. Surv. Circ.*, **486,** 15 pp.

Posey, J. W., and P. F. Clapp, 1964: Global distribution of normal surface albedo. *Geophis. Int.*, **4,** 33–48.

Randall, D. A., J. A. Abeles and T. G. Corsetti, 1985: Seasonal simulation of the planetary boundary layers and boundary-layer stratocumulus clouds with a general circulation model. *J. Atmos. Sci.*, **42,** 641–676.

Rasmusson, E. M., 1968: Atmospheric water vapour transport and the water balance of North America. Part II: Large-scale water balance investigations. *Mon. Wea. Rev.*, **96,** 720–734.

Salati, E., 1987: The forest and the hydrological cycle. *The Geophysiology of Amazonia.* R. E. Dickinson, Ed., Wiley and Sons, 273–296.

Sato, N., P. J. Sellers, D. A. Randall, E. K. Schneider, J. Shukla, J. L. Kinter III, Y.-T. Hou and E. Albertazzi, 1989: Implementing the Simple Biosphere Model (SiB) in a general circulation model: Methodology and Results. *NASA Contractor Report,* NASA HQ, p. 70. [Independence Ave., Washington, D.C. 20545]

Sela, J. G., 1980: Spectral modeling at the National Meteorological Center. *Mon. Wea. Rev.*, **108,** 1279–1292.

Sellers, P. J., 1985: Canopy reflectance, photosynthesis and transpiration. *Int. J. Remote Sens.*, **6,** 1335–1372.

——, Y. Mintz, Y. C. Sud and A. Dalcher, 1986: A simple biosphere model (SiB) for use within general circulation models. *J. Atmos. Sci.*, **43,** 505–531.

——, 1987: Modeling effects of vegetation on climate. *The Geophysiology of Amazonia.* R. E. Dickinson, Ed., Wiley and Sons, 244–264.

——, and J. L. Dorman, 1987: Testing the Simple Biosphere model (SiB) with point micrometeorological and biophysical data. *J. Climate Appl. Meteor.*, **26**(5), 622–651.

Sellers, W. D., 1965: *Physical Climatology.* The University of Chicago Press, 271 pp.

Shukla, J., and Y. Mintz, 1982: Influence of land-surface evapotranspiration on the earth's climate. *Science,* **215,** 1498–1501.

Shuttleworth, W. J., J. H. C. Gash, C. R. Lloyd, C. J. Moore, J. Roberts, A. O. Marques Filho, G. Fisch, V. P. Silva Filho, M. N. G. Ribeiro, L. C. B. Molion, L. A. De Sá, J. C. A. Nobre, O. M. R. Cabral, S. R. Patel and J. C. De Moraes, 1984a: Eddy correlation measurements of energy partition for Amazonian forest. *Quart. J. Roy. Meteor. Soc.*, **110,** 1143–1163.

—— et al., 1984b: Observation of radiation exchange above and below Amazonian forest. *Quart. J. Roy. Meteor. Soc.*, **110,** 1163–1169.

Sud, Y. C., and M. J. Fennessy, 1982: A study of the influence of surface albedo on July circulation in semi-arid regions using the GLAS GCM. *J. Climatol.*, **2,** 105–125.

——, and W. E. Smith, 1985: The influence of surface roughness of deserts on the July circulation. *Bound.-Layer Meteor.*, **33,** 15–40.

Swift, Jr., L. W., and W. T. Swank, 1975: Simulation of evapotranspiration and drainage from mature and clear-cut deciduous forests and young pine plantation. *Water Resour. Res.*, **11,** 667–673.

Tenhunen, J. D., O. L. Large, J. Gerbel, W. Beyschlag and J. A. Weber, 1984: Changes in photosynthetic capacity, carboxylation efficiency, and CO_2 compensation point associated with midday stomatal closure and midday depression of net CO_2 exchange of leaves of Querus suber. *Planta,* **162,** 193–203.

Tiedtke, M., 1984: The effect of penetrative cumulus convection on the large-scale flow in a general circulation model. *Beitr. Phys. Atmos.*, **57,** 216–239.

van der Ploeg, R. R., G. Tassone and J. von Hoyningen-Heune, 1980: The Joint Measuring Campaign 1979 in Ruthe (West Germany)—Description of Preliminary Data. European Econ. Comm., Joint Res. Cent., Ispra, Italy.

Walker, J. M., and P. R. Rowntree, 1977: The effect of soil moisture on circulation and rainfall in a tropical model. *Quart. J. Roy. Meteor. Soc.*, **103,** pp. 29–46.

Warrilow, D. A., 1986: The sensitivity of the UK Meteorological Office atmospheric general circulation model to recent changes in the parameterization of hydrology. ISLSCP, Proc. Int. Conf. ESA SP-248, ESA, Paris, France, 143–150.

Yamagishi, Y., 1980: Simulation of the air mass transformation process using a numerical model with detailed boundary layer parameterization. *J. Meteor. Soc. Japan,* **58,** 357–377.

Willmott, C. J., C. M. Rowe and Y. Mintz, 1985: Climatology of the terrestrial seasonal water cycle. *J. Climatol.*, **5,** 589–606.